Engineering Fracture Mechanics xxx (2016) xxx–xxx

Contents lists available at ScienceDirect

Engineering Fracture Mechanics

journal homepage: www.elsevier.com/locate/engfracmech

# A hierarchical multiscale cohesive zone model and simulation of dynamic fracture in metals

Dandan Lyu, Houfu Fan, Shaofan Li *

*Department of Civil and Environmental Engineering, University of California, Berkeley, CA 94720, USA*

ARTICLE INFO

*Article history:*
Received 20 February 2016
Received in revised form 5 June 2016
Accepted 6 June 2016
Available online xxxx

*Keywords:*
Cohesive zone model
Dynamic fracture
High-order Cauchy–Born rule
Multi-scale simulation
Polycrystalline solid

ABSTRACT

In this work, a hierarchical higher order multi-scale cohesive zone model (MCZM) is developed to simulate the fracture and crack propagation in crystalline solids. The main novelties of the present work are: (1) the hierarchical cohesive zone model is developed, and higher order Cauchy–Born rules (up to the third order) are employed to model different orders of the process zones; (2) the finite element bubble mode is added into the lower order element to capture high-order strain gradient effects in the conventional bilinear quadrilateral element; (3) Barycentric finite element method is used to construct shape functions for hexagonal shaped cohesive zones, and (4) realistic EAM potential is implemented to simulate fracture in metals. Numerical simulations of fracture and crack propagation in both monocrystalline solids and polycrystalline solids are performed. Results show that the crack propagation velocity is in general agreement with that of a corresponding molecular dynamics simulation. Moreover, the transition from intergranular fracture to transgranular fracture in polycrystalline solids is found to be sensitive to both the grain size and the relative grain strength. Finally, it is revealed that the proposed multiscale model can capture the spall fracture in a copper plate under high-speed impact.


## 1. Introduction

Crystalline materials are extensively used in many engineering branches such as aerospace, civil, mechanical engineering and materials science. The fracture of crystalline materials has been a critical issue in material design, synthesis and performance. The failure mechanics of materials [1,2] has been the focal point of material science. Considering the microstructure of polycrystalline solids, each grain has a unique crystallographic lattice orientation, shape and size, and the grain boundary between two grains is an inhomogeneous interphase with finite thickness. Many researchers, e.g. [3,4], have pointed out that the microstructure of polycrystalline solids has strong influences on how crack propagates in crystalline materials.

To model the fracture in crystalline solids, various methods have been developed at different scales. At macro-scale, there are many classical continuum damage models such as [5–8]. For instance, a temperature dependent creep damage model is proposed to investigate the damage of polycrystalline ice e.g. [9]. As a physical model of continuum damage, micromechanics-based void growth and coalescence models of polycrystalline solids have been extensively studied [10,11]. However, the main drawback of continuum damage models is that these models cannot describe the effects of microstructure characteristics such as lattice orientations and shapes [1,12]. At micro-scale, although ab initio methods or the first principle method are accurate, it is hardly practical to implement them to solve problems of large atomic systems

* Corresponding author.
*E-mail address:* shaofan@berkeley.edu (S. Li).

http://dx.doi.org/10.1016/j.engfracmech.2016.06.005
0013-7944/

Please cite this article in press as: Lyu D et al. A hierarchical multiscale cohesive zone model and simulation of dynamic fracture in metals. Engng Fract Mech (2016), http://dx.doi.org/10.1016/j.engfracmech.2016.06.005

**Nomenclature**

| | |
|---|---|
| $\mathbf{G}$ | gradient of deformation gradient |
| $\mathbf{H}$ | second order gradient of deformation gradient |
| $\mathbf{F}_e$ | element deformation gradient |
| $\mathbf{P}$ | the first Piola–Kirchhoff stress |
| $\phi$ | the atomistic potential |
| $\mathbf{Q}$ | the stress couple |
| $\mathbf{R}_i$ | undeformed lattice distance |
| $\mathbf{S}$ | the second Piola–Kirchhoff stress |
| $\sigma$ | the Cauchy stress |
| $\mathbf{U}$ | the second order stress couple |
| $\mathbf{u}(\mathbf{x})$ | the displacement field |
| $W$ | strain energy density |

because of the expensive computational cost [13]. Classical molecular dynamics (MD) increases the computational speed substantially but makes a compromise in accuracy compared to the first principle method e.g. [14]. Nevertheless, it is still impossible to conduct simulations of large scale atomistic systems for practical applications. From micro-scale to mesoscale, researchers have proposed many multi-scale methods in order to bridge the atomistic and continuum scales in a consistent manner. For example, a multi-scale boundary element method is proposed to investigate the degradation and fracture in polycrystalline materials [15]. Clayton [1] investigated dynamic thermomechanical response of a tungsten heavy alloy by considering cohesive interaction between adjacent grains.

Since middle 1990s [16], the cohesive zone model (CZM) has been widely used to simulate fractures in solid materials. It is a finite element version of classical cohesive crack model proposed by Dugdale [17] and Barrenblatt [18]. In this model, cohesive zone separates bulk elements automatically based on the magnitude of the external load, and it is governed by the traction-separation cohesive law between two bulk elements. This method has gained much popularity in computational materials failure analysis and mesoscale polycrystalline modeling. However, one prominent drawback of the conventional cohesive zone model lies in the fact that the bulk and cohesive zone constitutive relations are not related, and the empirical cohesive laws may not describe a mixed-mode decohesion mechanism of solids [19]. To overcome this problem, Zeng and Li [20] and Li et al. [21] proposed a multi-scale cohesive zone model, which employs an atomistic potential to construct the constitutive relation of bulk material using the Cauchy–Born rule. In particular, a depletion potential of the cohesive interface is constructed in accord with the atomistic potential inside the bulk material. These potentials naturally take into account the information of lattice microstructure, such as atom positions and lattice orientations. Subsequently, the multi-scale cohesive zone model was utilized to simulate many phenomenons in practice. For example, Qian and Li [2] adopted the multi-scale cohesive zone model to study the crack propagation in polycrystalline solids. Zeng and Li used this method to model composite materials [22]. He and Li [23] combined the embedded atom method (EAM) with cohesive zone model (CZM) to simulate the fracture and crack propagation at mesoscale and macroscale. Liu and Li [24] proposed a finite temperature multi-scale interphase zone model to simulate crack propagation of metallic materials. Fan and Li [25] employed the multi-scale cohesive zone model(MCZM) to study crack propagation in polycrystalline solids, by making use of the higher order Cauchy–Born rules of the same atomistic potential in both the cohesive interface and bulk elements.

There are several differences between the current work and that in [25]. In the original work of Fan and Li [25], a bilinear quadrilateral element was employed to model the cohesive zone element. The deformation inside the process zone is assumed to be inhomogeneous, and the second order Cauchy–Born rule is used to derive the constitutive relation. However, the bilinear quadrilateral element only provides bilinear polynomials, which cannot support the main part of the second order strain gradients, so that the effect by using second-order Cauchy–Born rule based constitutive relation is almost the same as that by using the first-order Cauchy–Born rule based constitutive relation. Therefore, in the present work, a bubble mode is added into the quadrilateral element to support high-order strain gradient effects. Moreover, through mathematical manipulation of integration by parts, an interface cohesive law that is capable of describing the lattice microstructure of the cohesive zone is derived.

In this work, the multi-scale cohesive zone model is constructed in a Lagrange type of the Galerkin finite element weak form formulation. Barycentric finite element method is used to construct shape functions and quadrature integration rules for hexagonal domains. Numerical simulations of fracture in crystalline and polycrystalline solids are carried out. The first example only considers the first-order process zone in polycrystalline solids, while both the first-order and second-order process zone are taken into account in crystalline solids for the second and third example. Finally, the effects of the grain size and the strength ratio between the intergranular fracture to transgranular fracture transition are investigated quantitatively. The critical strength ratio for the transition from intergranular fracture to transgranular fracture is given for different grain sizes.

Please cite this article in press as: Lyu D et al. A hierarchical multiscale cohesive zone model and simulation of dynamic fracture in metals. Engng Fract Mech (2016), http://dx.doi.org/10.1016/j.engfracmech.2016.06.005

This paper is organized as follows. Section 2 introduces the concept of multiscale cohesive zone model (MCZM). Section 3 presents the modeling of the polycrystalline structure. In Section 4, modeling of the multi-scale cohesive zone is provided. Section 5 focuses on constructing the Galerkin weak-form and the corresponding implementations. Several numerical examples are presented in Section 6. Finally, a few remarks are made in Section 7.

## 2. Multiscale cohesive zone model (MCZM)

From the viewpoint of the statistical mechanics, the multiscale cohesive zone model (MCZM) is a coarse grain model. In the MCZM, a global non-uniform deformation field is discretized into a set of bulk crystal elements with piece-wise uniform deformations, and they are connected by a network of process zone that contains many finite size cohesive elements of different orders, in which the deformations are highly non-uniform and nonlinear as shown in Fig. 1.

A comparison between the conventional cohesive zone model and the multiscale cohesive model is shown in Fig. 2. In the conventional cohesive zone model [16], the cohesive element is a pair of discrete cohesive surfaces with zero width or thickness, and two surface elements are glued together by prescribing certain cohesive laws between them. The introduction of the cohesive surface element is to allow discontinuity kinematics in finite element solution. While for the multiscale cohesive zone model, bulk elements with uniformed deformation are connected by finite-width cohesive zone element with nonlinear or non-uniform deformations.

From Fig. 1, one may find that the crystalline solid bock is decomposed into bulk crystal elements (0-th order process zone) and higher order cohesive zone (interphase) elements, in which the constitutive modeling for both bulk materials as well as cohesive zones are constructed based on the same atomistic potential and lattice microstructure inside. However, the order of the Cauchy–Born rules for the bulk crystal elements and the cohesive zone are different.

## 3. Modeling polycrystalline microstructure

In this work, *Centroidal Voronoi Tessellation* has been extensively utilized to create various random microstructure to investigate the effect of grain morphology on mechanical properties of polycrystalline solids e.g. [26,27,3]. In this work, the test specimens are generated by centroidal voronoi tessellation. As can be seen from Fig. 3, each Voronoi cell represents a grain and all edges of cells are considered to be grain boundaries. Fig. 6 shows triangular elements generated by using the Delaunay triangulation method inside each grain, which are treated as bulk elements. Cohesive zones are constructed on the interfaces of bulk elements. For the bulk elements and the cohesive zones in the same grain, they have the same lattice orientation. However, we randomly assign each grain a lattice orientation $\alpha^g$ in order to characterize the varying grain morphology. Here the superscript $g$ represents granular region and the superscript $gb$ denotes the zones on grain boundaries. Meanwhile, the lattice orientation of grain boundary zones $\alpha^{gb}$ can be assigned based on different assumptions. For the purpose of simplicity, the lattice orientation of a grain boundary zone is set to be the average of orientations of the two adjacent grains, i.e. $\alpha^{gb} = \frac{1}{2}(\alpha_A^g + \alpha_B^g)$, as shown in Fig. 3.

## 4. Constitutive modeling

In this section, we discuss how to derive the constitutive equation inside the bulk and cohesive zone by using the higher-order Cauchy–Born rule. Before deriving stress–strain relation, we first explain what is the Cauchy–Born rule.

### 4.1. Higher-order Cauchy–Born rules

In the following, we first lay out the hierarchical higher order Cauchy–Born rules up to the third order.

#### 4.1.1. The 1st order Cauchy–Born rule in the 0th order process zone (bulk element)

In a crystalline bulk element, say element $e$, which usually is a part of single crystal or a single grain, we assume that the deformation is uniform, and thus the deformation gradient inside the whole element is the same, i.e.

$$\mathbf{F}_e(\mathbf{X}) = \frac{\partial \mathbf{x}}{\partial \mathbf{X}}\Big|_{\mathbf{x}} = const., \quad \forall \mathbf{X} \in \Omega_e$$

Note that in the entire solid domain we have $\mathbf{F}_e, e = 1, 2, \ldots, n^b_{elem}$, where $n^b_{elem}$ is the total number of bulk (superscript) elements.

Then based on the first order Cauchy–Born rule, an arbitrary deformed chemical bond $\mathbf{r}_i$ between two atoms inside the element can be related to the original undeformed bond $\mathbf{R}_i$ as

$$\mathbf{r}_i = \mathbf{F}_e \cdot \mathbf{R}_i, i = 1, \ldots, n_b \tag{1}$$

where index $i$ denotes a chemical bond inside element $e$ and $n_b$ represents the total number of bonds the element. In practice, chemical bonds in a representative unit inside $\Omega_e$, $n_b$.

With these definitions, the strain energy density in the bulk element $e$ can be written as

Please cite this article in press as: Lyu D et al. A hierarchical multiscale cohesive zone model and simulation of dynamic fracture in metals. Engng Fract Mech (2016), http://dx.doi.org/10.1016/j.engfracmech.2016.06.005

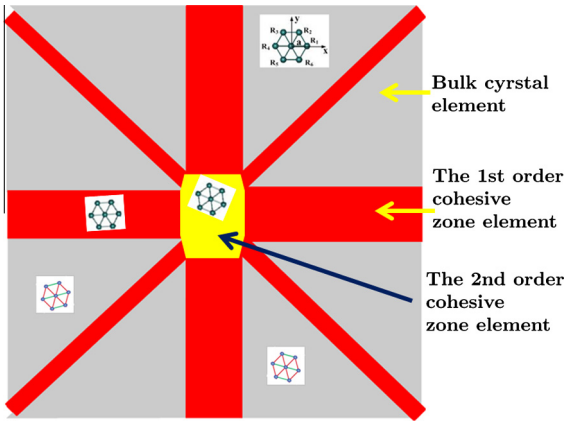


**Fig. 1.** Schematic illustration and local finite element mesh of MCZM.

$$W_{0e} = \frac{1}{2\Omega_0}\sum_{i=1}^{n_b}\phi(r_i) = \frac{1}{2\Omega_0}\sum_{i=1}^{n_b}\phi(\mathbf{F}_e\cdot\mathbf{R}_i) = W(\mathbf{F}_e), \tag{2}$$

where $n_b$ again indicates the number of neighboring bonds in a representative unit cell; $\Omega_0$ is the volume of the unit cell in the referential configuration; $\phi(r_i)$ is the atomistic potential, and $r_i = |\mathbf{r}_i|$ is the current length of bond $\mathbf{r}_i$ in the unit cell. The energy density expression (2) is formulated based on the first order Cauchy–Born rule (see Eq. (1)), and the first Piola–Kirchhoff stress tensor inside the bulk crystal element can be found by

$$\mathbf{P} = \frac{\partial W_{0e}}{\partial \mathbf{F}}\Big|_{\mathbf{F}_e}.$$

*4.1.2. The 2nd order Cauchy–Born rule in the 1st order process zone*

For the first-order process zone element, which is usually a rectangular strip between two adjacent sides of two bulk crystal elements, the second order Cauchy–Born rule is employed to establish the constitutive relation in it. The so-called second order Cauchy–Born rule assumes that in a representative 1st order process zone element $e$, a deformed chemical bond between two atoms may be expressed by the following expression,

$$\mathbf{r}_i = \mathbf{F}_e\cdot\mathbf{R}_i + \frac{1}{2}\mathbf{G}_e : (\mathbf{R}_i\otimes\mathbf{R}_i) \tag{3}$$

where

$$\mathbf{G}_e = \frac{\partial^2\mathbf{x}}{\partial\mathbf{X}\otimes\partial\mathbf{X}} = \frac{\partial\mathbf{F}_e}{\partial\mathbf{X}} = const. \quad \forall\mathbf{X}\in\Omega_e$$

Note that in this case, $\mathbf{F}_e \neq const$.

Taking into account the 1st order strain gradient effect on strain energy density, we may write the strain energy density in the 1st order process zone element $e$ as

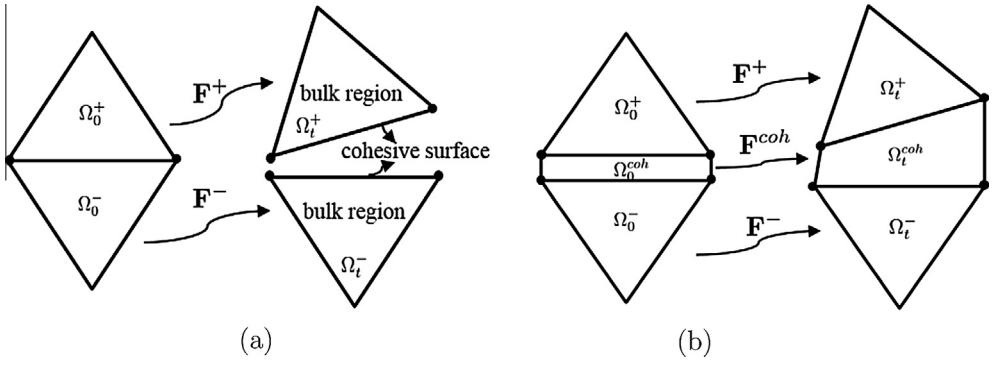


**Fig. 2.** Comparison of (a) conversional cohesive zone model and (b) multiscale cohesive zone model.

Please cite this article in press as: Lyu D et al. A hierarchical multiscale cohesive zone model and simulation of dynamic fracture in metals. Engng Fract Mech (2016), http://dx.doi.org/10.1016/j.engfracmech.2016.06.005

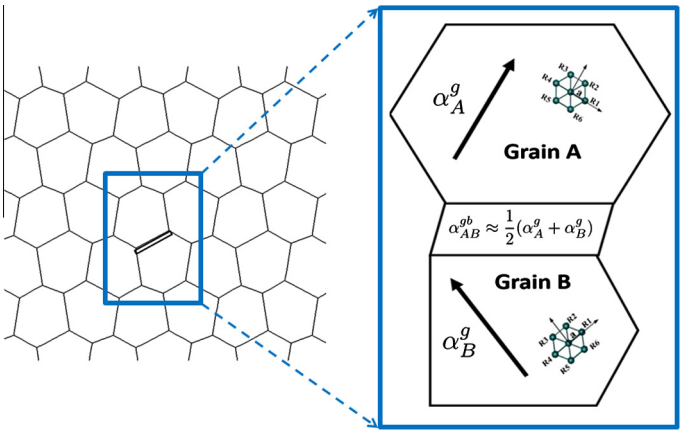


**Fig. 3.** Voronoi cell representation of polycrystal grains and orientations of grains and grain boundary.

$$W_{1e} = \frac{1}{2\Omega_0}\sum_{i=1}^{n_b}\phi(r_i) = \frac{1}{2\Omega_0}\sum_{i=1}^{n_b}\phi\left(\left|\mathbf{F}_e\cdot\mathbf{R}_i + \frac{1}{2}\mathbf{G}_e:(\mathbf{R}_i\otimes\mathbf{R}_i)\right|\right) = W(\mathbf{F}_e,\mathbf{G}_e), \tag{4}$$

which is based on the second order Cauchy–Born rule (see Eq. (3). Subsequently, the constitutive relation inside the 1st order process zone can be expressed as,

$$\mathbf{P} = \frac{\partial W_{1e}}{\partial \mathbf{F}}\Big|_{\mathbf{F}_e,\mathbf{G}_e} \quad \text{and} \quad \mathbf{Q} = \frac{\partial W_{1e}}{\partial \mathbf{G}}\Big|_{\mathbf{F}_e,\mathbf{G}_e}.$$

*4.1.3. The 3rd order Cauchy–Born rule in the 2nd order process zone*

For the second-order process zone element, which is either a hexagonal element or a rectangular element (see Figs. 13 and 18), the third-order Cauchy–Born rule is employed to derive its constitutive relation. In the third-order Cauchy–Born rule, a chemical bond can be expressed as

$$\mathbf{r}_i = \mathbf{F}_e\cdot\mathbf{R}_i + \frac{1}{2!}\mathbf{G}_e:(\mathbf{R}_i\otimes\mathbf{R}_i) + \frac{1}{3!}\mathbf{H}_e\dot{:}(\mathbf{R}_i\otimes\mathbf{R}_i\otimes\mathbf{R}_i), \tag{5}$$

where $i = 1,\ldots,n_b$ is the index of number of bonds in a unit cell, and

$$\mathbf{H}_e = \frac{\partial^3\mathbf{x}}{\partial\mathbf{X}\otimes\partial\mathbf{X}\otimes\partial\mathbf{X}} = \frac{\partial^2\mathbf{F}}{\partial\mathbf{X}\otimes\partial\mathbf{X}} = \frac{\partial\mathbf{G}}{\partial\mathbf{X}} = const. \quad \forall\mathbf{X}\in\Omega_e.$$

Note that the dot product operation defined in this paper has the following equivalent indicial notations,

$$\mathbf{F}\cdot\mathbf{R}_i = F_{mn}R_n\mathbf{e}_m, \quad \mathbf{G}:(\mathbf{R}_i\otimes\mathbf{R}_i) = G_{\ell mn}R_mR_n\mathbf{e}_\ell, \text{ and}$$

$$\mathbf{H}\dot{:}(\mathbf{R}_i\otimes\mathbf{R}_i\otimes\mathbf{R}_i) = H_{\ell mno}R_mR_nR_o\mathbf{e}_\ell, \quad \ell,m,n,o = 1,2,3$$

where $\mathbf{e}_\ell, \ell = 1,2,3$ are the unit base vectors of the Cartesian coordinates.

Following the similar argument mentioned above, we can show that the strain energy density in the second-order process zone element $e$ may be generally expressed in the form of

$$W_{2e} = W(\mathbf{F}_e,\mathbf{G}_e,\mathbf{H}_e).$$

Note that in this case $\mathbf{F}_e \neq const.$ and $\mathbf{G}_e \neq const.$

By taking into account the first and second order strain gradients, we can derive the constitutive relations in the 2nd order process zone as

$$\mathbf{P} = \frac{\partial W_{2e}}{\partial \mathbf{F}}\Big|_{\mathbf{F}_e,\mathbf{G}_e,\mathbf{H}_e}, \quad \mathbf{Q} = \frac{\partial W_{2e}}{\partial \mathbf{G}}\Big|_{\mathbf{F}_e,\mathbf{G}_e,\mathbf{H}_e} \quad \text{and} \quad \mathbf{U} = \frac{\partial W_{2e}}{\partial \mathbf{H}}\Big|_{\mathbf{F}_e,\mathbf{G}_e,\mathbf{H}_e}.$$

It is noted in passing that we have interchangeably used terms *process zone* and *cohesive zone*. In fact, there is a subtle difference between the two: the term *cohesive zone* mainly refers to interface or interphase zone, whereas the term *process zone* is a general term for the defect zone that not only refers to interface/interphase zone, but also refers to other types of defects such as voids, dislocation loops, and disclination zones.

Please cite this article in press as: Lyu D et al. A hierarchical multiscale cohesive zone model and simulation of dynamic fracture in metals. Engng Fract Mech (2016), http://dx.doi.org/10.1016/j.engfracmech.2016.06.005

### 4.2. Multiscale constitutive models

Different from [25], in this work, we simulate dynamic fracture in real materials, specifically in metallic materials. For metallic materials, we can use the atomistic potential based on the embedded atom method (EAM) to construct the free energy density function for the crystal solid under consideration,

$$W = \frac{1}{\Omega_0}\sum_{i=1}^{n_b}\left((1-\chi)F(\bar{\rho}_i) + \frac{1}{2}\chi\sum_{j\neq i}\phi(r_{ij})\right), \quad r_{ij} = |\mathbf{r}_j - \mathbf{r}_i|. \tag{6}$$

where $\chi$ is a weighting parameter between zero and one and $\phi(r_{ij})$ is the pairwise interaction function. Since $\phi(r_{ij})$ is always shared by two atoms, there is a coefficient of $\frac{1}{2}$ for the pairwise interaction function. $F(\bar{\rho}_i)$ is the embedded energy function and the host electron density $\bar{\rho}$ is a function of the electron density

$$\bar{\rho} = \sum_{j\neq i}\rho(r_{ij}).$$

For simplicity, in this paper, we only consider the crystal materials whose crystal lattices have only one atom inside the unit cell, i.e. the Bravais lattice. Under this restriction, the potential energy density inside a unit cell can be further simplified as

$$W = \frac{1}{\Omega_0}\left((1-\chi)F(\bar{\rho}) + \frac{1}{2}\chi\sum_{j}\phi(r_j)\right), \quad \bar{\rho} = \sum_{j}\rho(r_j), \tag{7}$$

where $i,j = 1,2,\ldots,n_b$ is the bond number of pair potential in a unit cell. With the above free energy density, the first Piola–Kichhoff stress can be obtained as

$$\mathbf{P} = \frac{\partial W}{\partial \mathbf{F}} = \frac{1}{\Omega_0}\sum_{j=1}^{n_b}\left((1-\chi)F'(\bar{\rho})\rho'(r_j) + \frac{1}{2}\chi\phi'(r_j)\right)\frac{\mathbf{r}_j\otimes\mathbf{R}_j}{r_j}. \tag{8}$$

Other useful formulas for stresses and high order stress couples can also be derived as,

$$\mathbf{S} = \frac{1}{\Omega_0}\sum_{j=1}^{n_b}\left((1-\chi)F'(\bar{\rho})\rho'(r_j) + \frac{1}{2}\chi\phi'(r_j)\right)\frac{\mathbf{R}_j\otimes\mathbf{R}_j}{r_j}, \tag{9}$$

$$\boldsymbol{\sigma} = \frac{1}{\Omega_0}\sum_{j=1}^{n_b}\left((1-\chi)F'(\bar{\rho})\rho'(r_j) + \frac{1}{2}\chi\phi'(r_j)\right)\frac{\mathbf{r}_j\otimes\mathbf{r}_j}{r_j}, \tag{10}$$

$$\mathbf{Q} = \frac{\partial W}{\partial \mathbf{G}} = \frac{1}{2\Omega_0}\sum_{j=1}^{n_b}\left((1-\chi)F'(\bar{\rho})\rho'(r_j) + \frac{1}{2}\chi\phi'(r_j)\right)\frac{\mathbf{r}_j\otimes\mathbf{R}_j\otimes\mathbf{R}_j}{r_j}, \tag{11}$$

$$\mathbf{U} = \frac{\partial W}{\partial \mathbf{H}} = \frac{1}{6\Omega_0}\sum_{j=1}^{n_b}\left((1-\chi)F'(\bar{\rho})\rho'(r_j) + \frac{1}{2}\chi\phi'(r_j)\right)\frac{\mathbf{r}_j\otimes\mathbf{R}_j\otimes\mathbf{R}_j\otimes\mathbf{R}_j}{r_j}. \tag{12}$$

Note that from Fig. 3 one may find that the stress tensor calculated based on the above Cauchy–Born rule depends on each grain's lattice orientation.

### 4.3. Bubble mode and benchmark test

In MCZM, the same atomistic potential is used to construct constitutive relations for different types of elements, but different types of elements may have different kinematic and constitutive constrains. i.e. the bulk element only supports uniform deformation, which is modeled by the first-order Cauchy–Born rule. Non-uniform deformation is assumed to be confined in the cohesive zone elements, which is modeled by the second or third order Cauchy–Born rule. To have a quantitative view on the difference of the constitutive relations between the bulk and cohesive elements, a benchmark test is performed. Fig. 4 shows the schematic of a cohesive element sandwiched by two triangular bulk elements. The first-order Cauchy–Born rule and the second-order Cauchy–Born rule are used to model the bulk and cohesive zone element, respectively. The benchmark test is an uniaxial test: an external load is gradually applied at the top nodes of two bulk elements, during which the relative displacement between the two nodes is measured.

Given that the shape functions of the four-node bilinear quadrilateral element (Q4) only contains bilinear polynomials, and it does not have the majority of the second order derivatives. A bubble mode $N_5(\mathbf{X})$ is added into the Q4 element to support non-linear deformation that is required in the constitutive equation modeled by the second-order Cauchy–Born rule. The four-node bilinear quadrilateral element shape functions with the bubble mode are given as follows,

Please cite this article in press as: Lyu D et al. A hierarchical multiscale cohesive zone model and simulation of dynamic fracture in metals. Engng Fract Mech (2016), http://dx.doi.org/10.1016/j.engfracmech.2016.06.005

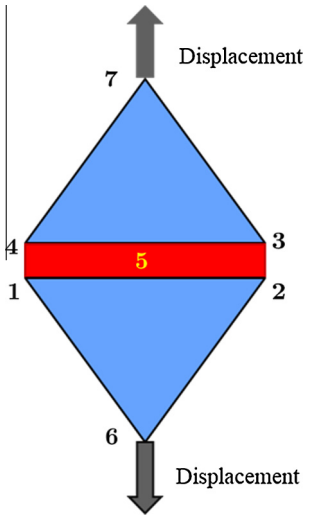


**Fig. 4.** Schematic illustration of the benchmark test setting.

$$
\begin{aligned}
N_1(\xi,\eta) &= \tfrac{1}{4}(1-\xi)(1-\eta) - \tfrac{1}{4}N_5(\xi,\eta)\\
N_2(\xi,\eta) &= \tfrac{1}{4}(1+\xi)(1-\eta) - \tfrac{1}{4}N_5(\xi,\eta)\\
N_3(\xi,\eta) &= \tfrac{1}{4}(1+\xi)(1+\eta) - \tfrac{1}{4}N_5(\xi,\eta)\\
N_4(\xi,\eta) &= \tfrac{1}{4}(1-\xi)(1-\eta) - \tfrac{1}{4}N_5(\xi,\eta)\\
N_5(\xi,\eta) &= (1-\xi^2)(1-\eta^2),
\end{aligned}
$$

and the element interpolation field becomes

$$\mathbf{u}(\mathbf{X}) = N_1(\mathbf{X})\mathbf{u}_1 + N_2(\mathbf{X})\mathbf{u}_2 + N_3(\mathbf{X})\mathbf{u}_3 + N_4(\mathbf{X})\mathbf{u}_4 + N_5(\mathbf{X})\mathbf{u}_5, \tag{13}$$

where the interpolation field is within the 1st order cohesive zone.

There are different ways to determine the nodal displacement of the bubble node. Without introducing new degrees of freedom, we adopt the following two different approaches.

(a) Case 1: the displacements of the bubble mode equal the average displacements of the four nodes in the cohesive zone element, i.e.

$$\mathbf{u}_5 = \frac{1}{4}\sum_{i=1}^{4}\mathbf{u}_i;$$

(b) Case 2: the displacements of the bubble mode equal the average displacements of the six nodes of the bulk and the cohesive zone element, i.e.

$$\mathbf{u}_5 = \frac{1}{6}\left(\sum_{i=1}^{4}\mathbf{u}_i + \mathbf{u}_6 + \mathbf{u}_7\right).$$

In the computations, the first order Cauchy–Born (CB) rule is used in two triangular bulk elements, whereas in the cohesive zone element (the red[1] one) either the first order CB rule is used or the second order CB rule is used. The load-deflection curves are plotted in Fig. 5. As can be seen, the peak value based on the first-order CB rule is higher than that of the second-order CB rule for Case 2, which implies that the cohesive zone element is relatively weaker than the bulk element, and thus in simulations the cohesive zone will always fail or break first. However, for Case 1, which treats the average displacement of the four nodes of the cohesive zone element as that of the bubble mode, the peak values calculated based on the first and second-order Cauchy–Born rules are almost the same. The reason is that under the kinematic assumption of Case 1 the bubble mode effect is canceled out, and the deformation in the cohesive zone element is a linear homogeneous displacement field which has no difference in stress value prediction when using the first-order and second-order Cauchy–Born rule to calculate stress. The results of the benchmark test clearly show that the higher order strain gradient used in a constitutive model, the lower strength of the constitutive model.

[1] For interpretation of color in Fig. 4, the reader is referred to the web version of this article.

Please cite this article in press as: Lyu D et al. A hierarchical multiscale cohesive zone model and simulation of dynamic fracture in metals. Engng Fract Mech (2016), http://dx.doi.org/10.1016/j.engfracmech.2016.06.005

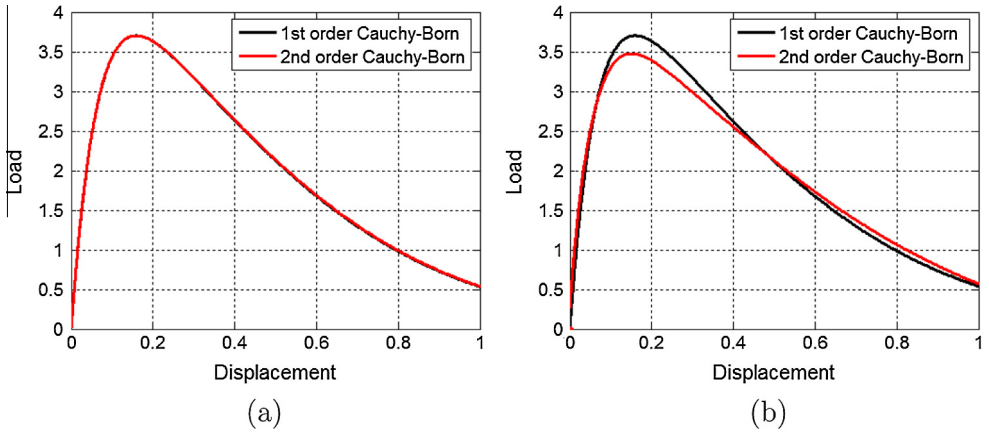


**Fig. 5.** Constitutive behaviors of the first order (bulk) and second order (cohesive) cohesive zones: (a) Case 1 and (b) Case 2.

## 5. FEM implementations

In this Section, we discuss the related multiscale finite element formulation, and its implementation. The total energy of the polycrystalline solid is

$$\mathcal{K} = \int_{\Omega} \frac{1}{2} \rho \dot{\mathbf{u}} \cdot \dot{\mathbf{u}} dV \tag{14}$$

where $\rho$ is the mass density, $\dot{\mathbf{u}}$ is the velocity field in the continuum. The internal free energy of crystal continuum can be expressed as

$$\mathcal{W}_{int} = \int_{\Omega} W(\mathbf{F}, \mathbf{G}, \mathbf{H}) dV \tag{15}$$

where $W(\cdot)$ is the strain gradient energy density. To derive finite element formulation, we consider Hamilton's principle, in which adopted in terms of displacement variation between the fixed time interval from $t_0$ to $t_1$,

$$\delta \int_{t_0}^{t_1} (\mathcal{W}_{ext} + \mathcal{W}_{int} - \mathcal{K}) = 0 \tag{16}$$

where $\mathcal{W}_{ext}$ is the external potential energy. The variation of kinetic energy is,

$$\delta \mathcal{K} = \int_{\Omega} \rho \dot{\mathbf{u}} \cdot \delta \dot{\mathbf{u}} dV \tag{17}$$

Via integration by parts, we have

$$\int_{t_1}^{t_2} \rho \dot{\mathbf{u}} \cdot \delta \dot{\mathbf{u}} dt = \rho \dot{\mathbf{u}} \cdot \delta \mathbf{u} \Big|_{t_1}^{t_2} - \int_{t_1}^{t_2} \rho \ddot{\mathbf{u}} \cdot \delta \dot{\mathbf{u}} dt = - \int_{t_1}^{t_2} \rho \ddot{\mathbf{u}} \cdot \delta \dot{\mathbf{u}} dt \tag{18}$$

The first variation of the internal energy is

$$\delta \mathcal{W}_{int} = \int_{\Omega} \left[ \mathbf{P}(\phi) : \delta \mathbf{F} + \mathbf{Q}(\phi) \vdots \delta \mathbf{G} + \mathbf{U}(\phi) :: \delta \mathbf{H} \right] dV \tag{19}$$

where the symbols $:, \vdots$ and $::$ denote tensor dot product operators. They represent double contraction, triple contraction and the fourth contraction, which are used for second-order, third-order and fourth-order tensor dot product calculations, respectively. In particular, an equivalent indicial notation for the last term in (19) is

$$\mathbf{U} :: \delta \mathbf{H} = U_{ijk\ell} \delta H_{ijk\ell}.$$

The first variation of the external potential energy is calculated as

$$\delta \mathcal{W}_{ext} = - \int_{\Omega} \mathbf{b} \cdot \delta \mathbf{u} dV - \int_{\partial \Omega_t} \bar{\mathbf{T}} \cdot \delta \mathbf{u} dS \tag{20}$$

where $\mathbf{b}$ is the body force and $\bar{\mathbf{T}}$ is the traction vector on $\partial \Omega_t$.

Please cite this article in press as: Lyu D et al. A hierarchical multiscale cohesive zone model and simulation of dynamic fracture in metals. Engng Fract Mech (2016), http://dx.doi.org/10.1016/j.engfracmech.2016.06.005

The Galerkin weak-form of the MCZM can be written as

$$\int_{\Omega}\left[\rho\ddot{\mathbf{u}}\cdot\delta\mathbf{u}+\mathbf{P}(\phi):\delta\mathbf{F}+\mathbf{Q}(\phi)\vdots\delta\mathbf{G}+\mathbf{U}(\phi)::\delta\mathbf{H}\right]dV=\int_{\Omega}\mathbf{b}\cdot\delta\mathbf{u}dV+\int_{\partial\Omega_t}\bar{\mathbf{T}}\cdot\delta\mathbf{u}dS. \tag{21}$$

Successive integration by parts for the internal energy yields

$$\begin{aligned}\delta\mathcal{W}_{int}=&-\int_{\Omega}\nabla_X\cdot[\mathbf{P}-\nabla_X\cdot(\mathbf{Q}-\nabla_X\cdot\mathbf{U})]\cdot\delta\mathbf{u}dV+\int_{\partial\Omega}\{[\mathbf{P}-\nabla_X\cdot(\mathbf{Q}-\nabla_X\cdot\mathbf{U})]\cdot\mathbf{N}\}\cdot\delta\mathbf{u}dS\\&+\int_{\partial\Omega}[(\mathbf{Q}-\nabla_X\cdot\mathbf{U})\cdot\mathbf{N}]:\delta\mathbf{F}dS+\int_{\partial\Omega}(\mathbf{U}\cdot\mathbf{N})\vdots\delta\mathbf{G}dS,\end{aligned} \tag{22}$$

where the term for bulk element will disappear by taking account into the inertia and body force in the cohesive zone,

$$\nabla_X\cdot(\mathbf{P}-\nabla_X\cdot(\mathbf{Q}-\nabla_X\cdot\mathbf{U}))+\mathbf{b}=\rho\ddot{\mathbf{u}},\quad\forall\mathbf{X}\in\Omega_c. \tag{23}$$

Considering the assumption that the crystalline solid is surrounded by a uniformly deformed environment, that is

$$\delta\mathbf{F}=0,\quad\delta\mathbf{G}=0,\ \forall\mathbf{X}\in\partial\mathbf{V}.$$

Then the virtual work of the internal cohesive force can be simplified as

$$\delta\mathcal{W}_{coh}=\int_{\partial\Omega}[(\mathbf{P}-\nabla_X\cdot(\mathbf{Q}-\nabla_X\cdot\mathbf{U}))\cdot\mathbf{N}]\cdot\delta\mathbf{u}ds, \tag{24}$$

where the divergence of the second-order and the third order stress tensors can be directly derived analytically through Eqs. (11) and (12) as

$$\begin{aligned}\nabla_X\cdot\mathbf{Q}=&\frac{1}{2\Omega_0}\sum_{j=1}^{n_b}\left[(1-\chi)F''(\bar{\rho})\rho'^2(r_j)+(1-\chi)F(\bar{\rho})\rho''(r_j)+\frac{1}{2}\chi\phi''(r_j)\right]\\&\left[\mathbf{G}:(\mathbf{R}_j\otimes\mathbf{R}_j)\otimes\mathbf{R}_j+\frac{1}{2}\mathbf{H}\vdots(\mathbf{R}_j\otimes\mathbf{R}_j\otimes\mathbf{R}_j)\otimes\mathbf{R}_j\right]\end{aligned} \tag{25}$$

and

$$\begin{aligned}\nabla_X\cdot\mathbf{U}=&\frac{1}{6\Omega_0}\sum_{j=1}^{n_b}\left[(1-\chi)F''(\bar{\rho})\rho'^2(r_j)+(1-\chi)F(\bar{\rho})\rho''(r_j)+\frac{1}{2}\chi\phi''(r_j)\right]\\&\left[\mathbf{G}:(\mathbf{R}_j\otimes\mathbf{R}_j)\otimes\mathbf{R}_j\otimes\mathbf{R}_j+\frac{1}{2}\mathbf{H}\vdots(\mathbf{R}_j\otimes\mathbf{R}_j\otimes\mathbf{R}_j)\otimes\mathbf{R}_j\otimes\mathbf{R}_j\right]\end{aligned} \tag{26}$$

As shown in Eqs. (25) and (26), the divergence of the second order and the third order stress tensors are associated with the derivative of the deformation gradient, which requires the second and third derivatives of FEM shape functions in explicit expressions. That is exactly why a bubble mode is added into the bilinear quadrilateral element as shown in the benchmark test.

Consider the following local FEM interpolation function in a generic element

$$\mathbf{u}^h(\mathbf{X})=\sum_{I=1}^{n_{node}}N_I(\mathbf{X})\mathbf{d}_I \tag{27}$$

By substituting FEM shape function into the Galerkin weak form and considering the integration on the surface, one can obtain the discrete equations of motion as,

$$\mathbf{M}\ddot{\mathbf{d}}+\mathbf{f}^{int}(\mathbf{d})+\mathbf{f}^{cohe}(\mathbf{d})=\mathbf{f}^{ext}, \tag{28}$$

where

$$\begin{aligned}\mathbf{M}&=\mathcal{A}_{e=1}^{n_{elem}^b}\int_{B_0^e}\rho_0\mathbf{N}^{eT}\mathbf{N}^e dV\\\mathbf{f}^{int}&=\mathcal{A}_{e=1}^{n_{elem}}\int_{B_0^e}\mathbf{B}^{eT}\mathbf{P}^e(\mathbf{d})dV\\\mathbf{f}^{ext}&=\mathcal{A}_{e=1}^{n_{elem}}\left\{\int_{B_0^e}\mathbf{N}^{eT}\mathbf{B}^e dV+\int_{\partial_t B_0^e}\mathbf{N}^{eT}\bar{\mathbf{T}}^e dS\right\}\\\mathbf{f}^{cohe}&=\mathcal{A}_{e=1}^{n_{elem}^c}\left\{\int_{\partial\mathcal{C}_o^e}[(\mathbf{P}-\nabla_X\cdot(\mathbf{Q}-\nabla_X\cdot\mathbf{U}))\cdot\mathbf{N}]\cdot\mathbf{N}^{eT}dS\right\}\end{aligned}$$

in which $\mathcal{A}$ is the element assembly operator, $\mathbf{N}^e$ is the element shape function matrix, $\mathbf{B}^e$ is the element B-matrix.

**Remark 5.1.** The Newmark-$\beta$ method with $\beta=0,\gamma=0.5$ [28] is used as the explicit time integration scheme. The traction force $\mathbf{T}$ in the above equation is defined as follows:

$$\mathbf{T}:=(\mathbf{P}-\nabla_X\cdot(\mathbf{Q}-\nabla_X\cdot\mathbf{U}))\cdot\mathbf{N},\quad\forall\mathbf{X}\in\Omega_c,$$

Please cite this article in press as: Lyu D et al. A hierarchical multiscale cohesive zone model and simulation of dynamic fracture in metals. Engng Fract Mech (2016), http://dx.doi.org/10.1016/j.engfracmech.2016.06.005

which means that it is a higher order traction force. A higher order interface cohesive zone is constructed, whose constitutive relation may be derived form the atomistic potential by considering the lattice microstructure inside the cohesive zone [25].

## 6. Numerical examples

In this Section, we present several numerical simulation examples of dynamic crack propagation in polycrystalline and crystalline solids to validate the proposed higher order multiscale cohesive zone model. The first example is the two-scale cohesive zone modeling of dynamic fracture in a polycrystalline solid, in which only the first-order process zone is considered in the simulation. Meanwhile, the effects of the grain size and the strength ratio on the intergranular fracture to transgranular fracture transition are studied and discussed. In the second example, a three-scale cohesive zone model is employed to study dynamic fracture in a single crystal, in which the first and second order process zones are used in numerical simulations. We have compared the results obtained from the multiscale cohesive zone model with those obtained from molecular dynamics simulations. The third example investigates the spall fracture in a copper plate under high-speed by using a three-scale cohesive zone model.

### 6.1. Example I: Two-scale cohesive zone modeling of crack propagation

This example intends to demonstrate the effectiveness of the proposed method in simulation of the crack propagation in polycrystalline solids by considering only the first-order process zone. As shown in Fig. 6, a rectangular plate (2 mm × 2 mm) is subjected to unilateral tension in Y direction. Using the multi-scale cohesive zone method, this plate consists of 121 grains and 2376 bulk elements (see Fig. 6), which ultimately contains 3484 first-order process zone elements in this model. Along grain boundaries, a pre-crack is created in the left middle part of this plate. The simulation time step is set to be $\Delta t = 1 \times 10^{-10}$ s. In this example, both the bulk and cohesive zone element adopt the same inter-atomic potential—the 12–6 Lennard-Jones potential,

$$\phi = 4\epsilon\left[\left(\frac{\sigma}{r}\right)^{12} - \left(\frac{\sigma}{r}\right)^{6}\right] \tag{29}$$

where $\epsilon$ is the depth of the potential well, $r$ is the atomistic bond length, and $\sigma$ is the finite distance at which the atomistic potential is zero.

Buban et al. (2006) [29] demonstrated that grain boundaries are generally weaker than grains due to the atomic-scale defects on grain boundaries. In this paper, strength of the process zone is characterized by both the atomistic bond strength and its nonlinear deformation measure. To study the effects of cohesive strength, we first consider the case that the strength of the cohesive zones inside the grains is much higher than that of the grain boundaries, for instance, $3\epsilon^{gb}_{depl} = \epsilon^{g}_{depl}$. As shown in Fig. 7, the crack path follows exactly along the grain boundaries.

#### 6.1.1. Effects of cohesive strength ratio on fracture pattern

In this section, the effects of cohesive zone strength along grain boundaries and in grain cells on crack path are investigated. The cohesive strength ratio is denoted as $R_s = \epsilon^{gb}/\epsilon^{g}$, where $\epsilon^{g}$ represents the width of the potential in the process zones inside the grains and $\epsilon^{gb}$ denotes the width of the potential in the process zone along the grain boundaries. Several cases of $R_s$ are considered, such as 0.4, 0.5, 0.6, 0.7, 0.75, and 0.8. As shown in Fig. 8, as $R_s$ increases to 0.75, the crack begins to transform from intergranular fracture to transgranular fracture.

#### 6.1.2. Effects of grain size

To investigate the effects of grain size, two additional polycrystalline microstructures with 225 and 361 grains are generated, as shown in Fig. 9. Figs. 10 and 11 offer the simulation results at different cohesive strength ratio for 225 and 361 grains, respectively. It can be clearly seen that the grain size has influences on the fracture pattern transition in that the transition occurs at strength ratio $R_s = 0.9$ for 225 grains and increases to 0.95 for 361 grains. That is to say, the critical strength ratio for the transition from intergranular fracture to transgranular fracture increases as the grain size decreases. One possible explanation is that as the grain size decreases, the number of grain boundaries will increase. Hence it is more likely for the crack to propagate along the grain boundary, which is consistent with the conclusion made in [30] using a different simulation method.

Based on the numerical study, the following conclusions may be drawn:

(1) If the strength of the cohesive zone inside the grains is much higher than that of the grain boundaries, the crack path follows along the grain boundaries (see: Fig. 7).
(2) The strength ratio $R_s$ plays an important role in the fracture pattern. For example of the case of 121 grains, when $R_s$ increases to 0.8, the crack pattern begins to change from intergranular fracture to transgranular fracture.
(3) Simulation results of two additional structures with different grain sizes show that crack pattern is sensitive to the grain size (see Figs. 10 and 11). The transition occurs at strength ratio $R_s = 0.8$ for 121 grains, $R_s = 0.9$ for 225 grains, and $R_s$ threshold increases to 0.95 for 361 grains.

Please cite this article in press as: Lyu D et al. A hierarchical multiscale cohesive zone model and simulation of dynamic fracture in metals. Engng Fract Mech (2016), http://dx.doi.org/10.1016/j.engfracmech.2016.06.005

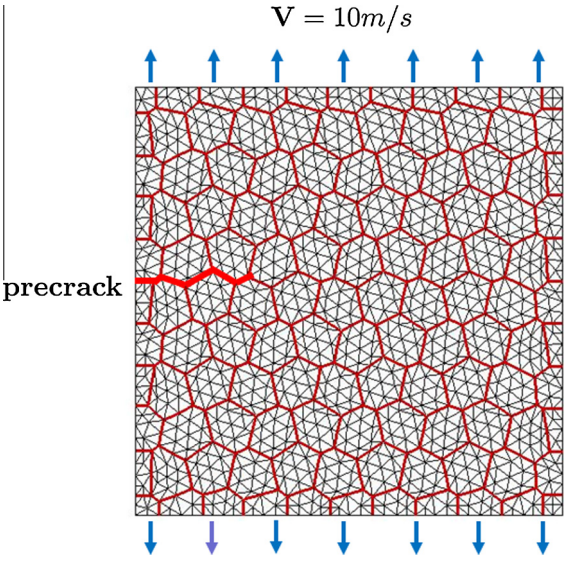


**Fig. 6.** Problem setting (Example I): uniaxial tension of a polycrystal specimen.

### 6.2. Example II: Three-scale cohesive zone modeling of crack propagation

In the second example, we present a study of three-scale cohesive zone modeling and simulation of dynamic fracture in a single crystal Copper. The bulk crystal element is treated as the zero-th order process zone, i.e. a non-defect identity; The interphase zone is modeled as the first order process zone, and the potential void zone as the second order process zone. The simulation specimen and its boundary condition are shown in Fig. 12.

To validate the method, the simulation results are compared with that of corresponding molecular dynamics simulation [31]. Since the (1 1 1) plane is the most susceptible slip plane in the FCC single crystal, so that the material on (1 1 1) plane must be weaker than that of bulk crystals. Therefore we would like to study the crack propagation within the (1 1 1) plane. As shown in Fig. 12, a high strain rate boundary condition is prescribed to initiate mode-I fracture. The finite element mesh contains the 0th (triangular element), 1st (rectangular element) and 2nd (honeycomb element) order process-zone elements, which are shown in the zoomed region of Fig. 12. Details of process zone mesh are provided in Fig. 13. At each vertex, there is one triangle, two rectangles and one hexagon. In this example, it is assumed that bulk elements only contain uniform deformations, which are described by the first-order Cauchy–Born rule. The rectangular and honeycomb elements can support non-uniform deformations, which are modeled by the second-order and third-order Cauchy-born rules.

#### 6.2.1. Embedded atom method (EAM) potential

In this example, an analytical EAM potential is adopted to describe material constitutive relation in the fracture simulation, which was used before in the molecular dynamic simulations e.g. [31]. The EAM potential is explicitly given as,

$$W = \frac{1}{\Omega_0}\sum_{i=1}^{n_b}[(1-\chi)F(\bar{\rho}_i) + \frac{1}{2}\chi\sum_{j\neq i}\phi(r_{ij})], \quad \bar{\rho}_i = \sum_{j\neq i}\rho(r_{ij}), \tag{30}$$

where $\chi$ is a weighting parameter between zero and one; the parameter $\chi = \frac{1}{3}$ is set based on the embedded atom method [32]; $F(\bar{\rho})$ is the embedded energy function; and $\phi(r)$ is the pairwise interaction function, whose expression can be written as follows:

$$F(\bar{\rho}) = \epsilon\frac{d(d+1)}{2}e\bar{\rho}\ln\bar{\rho} \tag{31}$$

and

$$\phi(r) = \begin{cases} \chi\psi(r), & r < r_{spl} \\ \chi\left\{\psi(r_{spl}) + \frac{\partial\psi}{\partial r}(r_{spl})(r-r_{spl}) - \frac{1}{6}A(r-r_{max})^3\right\}, & r_{spl} \leqslant r < r_{max} \\ 0, & r_{max} \leqslant r \end{cases} \tag{32}$$

where $r_{spl}$ is the reflection point in the potential; $r_{max}$ is the cutoff distance; and the potential function can be of different types based on specific problems. In this example, we choose

Please cite this article in press as: Lyu D et al. A hierarchical multiscale cohesive zone model and simulation of dynamic fracture in metals. Engng Fract Mech (2016), http://dx.doi.org/10.1016/j.engfracmech.2016.06.005

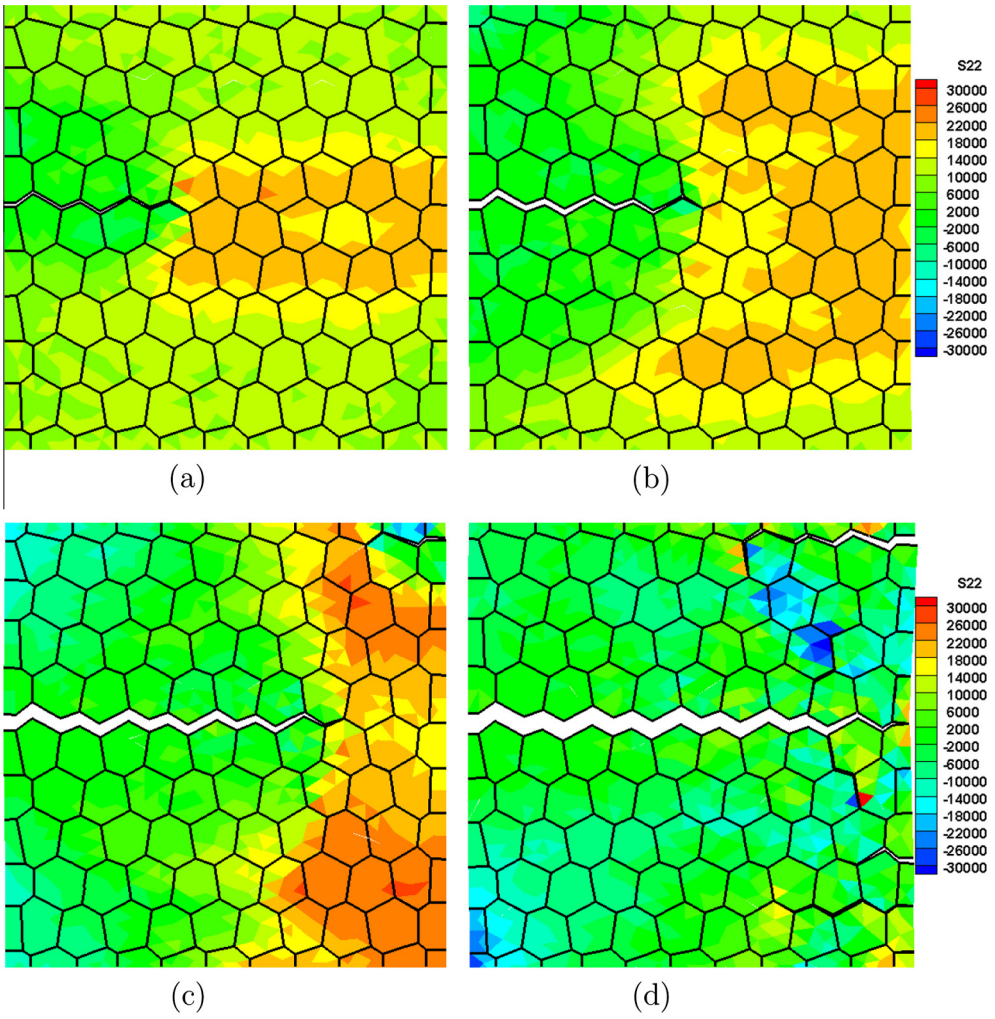


**Fig. 7.** Crack propagates along grain boundaries: (a) $t = 1.5$ μs; (b) $t = 2.0$ μs; (c) $t = 3.0$ μs, and (d) $t = 4.0$ μs.

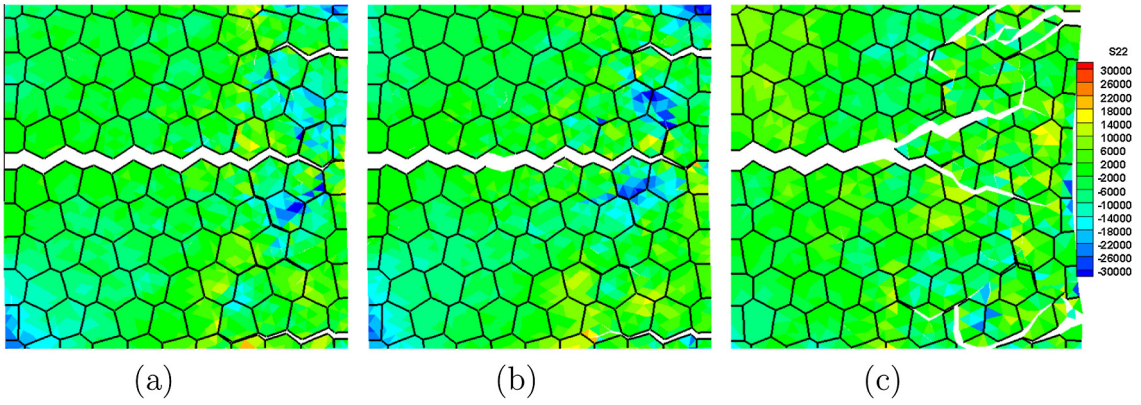


**Fig. 8.** Stress distribution of fractures in a polycrystalline solid with different strength ratios: (a)$R_s = 0.6$ (intergranular); (b)$R_s = 0.75$ (intergranular); and (c)$R_s = 0.8$ (transgranular).

Please cite this article in press as: Lyu D et al. A hierarchical multiscale cohesive zone model and simulation of dynamic fracture in metals. Engng Fract Mech (2016), http://dx.doi.org/10.1016/j.engfracmech.2016.06.005

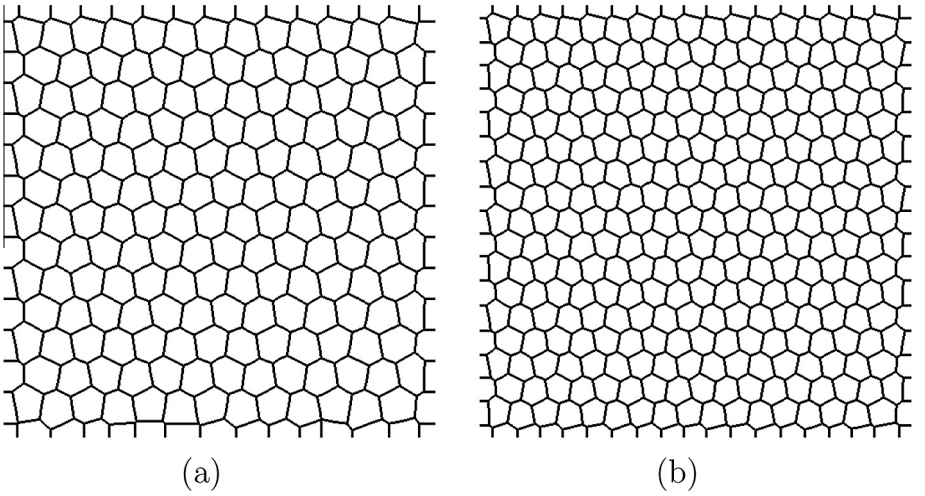


**Fig. 9.** Voronoi cells with different grain size: (a) Voronoi cell (225 grains, Poly 225); (b) Voronoi cell (361 grains, Poly 361).

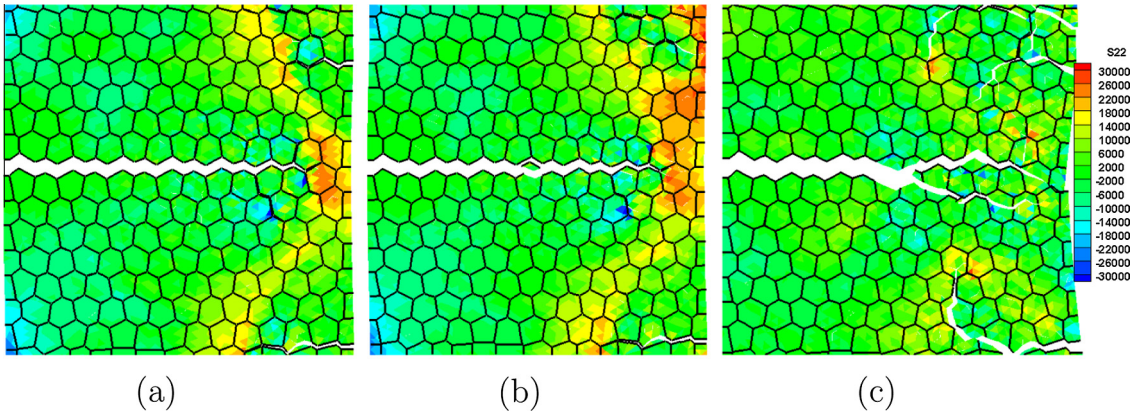


**Fig. 10.** Simulated stress distributions in the fractured polycrystalline solid with different strength ratios (225 grains): (a)$R_s = 0.75$ (intergranular); (b)$R_s = 0.8$ (intergranular); (c)$R_s = 0.9$ (transgranular).

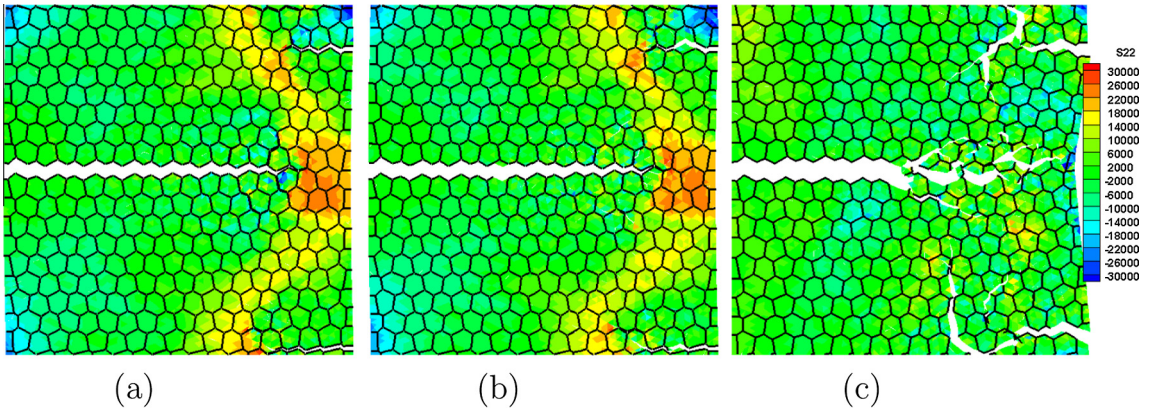


**Fig. 11.** Simulated stress distributions in the fractured polycrystalline solid with different strength ratios (361 grains): (a) $R_s = 0.75$ (intergranular); (b) $R_s = 0.85$ (intergranular); (c) $R_s = 0.95$(transgranular).

Please cite this article in press as: Lyu D et al. A hierarchical multiscale cohesive zone model and simulation of dynamic fracture in metals. Engng Fract Mech (2016), http://dx.doi.org/10.1016/j.engfracmech.2016.06.005

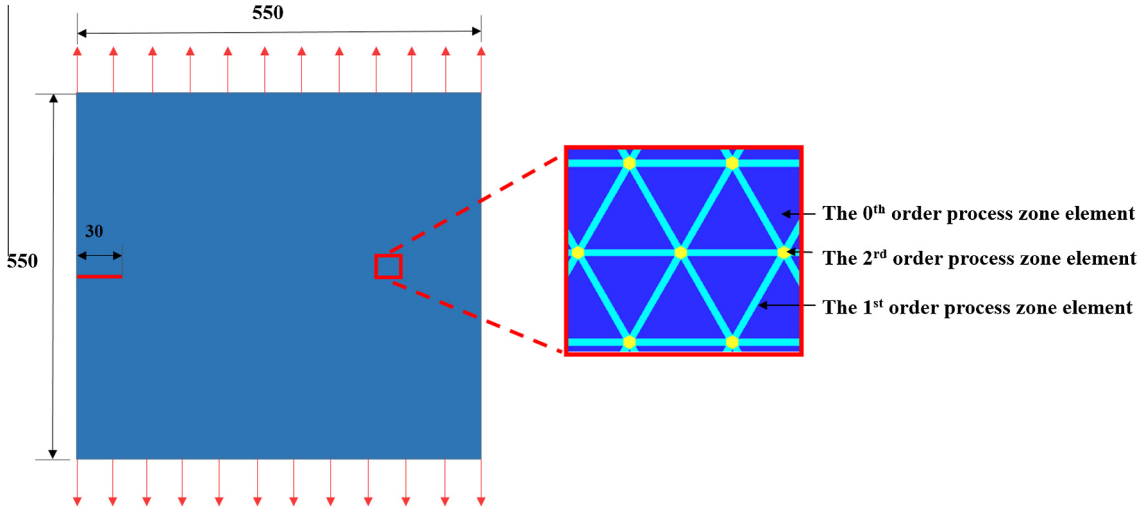


**Fig. 12.** Schematic illustration of Example II and multiscale process zone mesh.

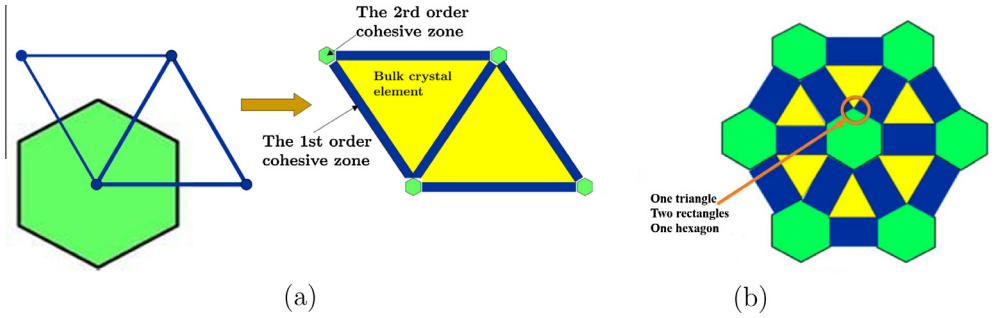


**Fig. 13.** The process of process zone tiling: (1) Yellow region: the zero-th order process zone; (2) Blue region: the 1st process zone, and (3) Green region: the 2nd process zone. (For interpretation of the references to color in this figure legend, the reader is referred to the web version of this article.)

$$\psi(r) = \epsilon\left[\left(\frac{r_0}{r}\right)^{12} - 2\left(\frac{r_0}{r}\right)^{6}\right], \tag{33}$$

and the constant A in Eq. (32) is defined as

$$A = \frac{8\left(\frac{\partial\psi}{\partial r}(r_{spl})\right)^3}{9(\psi(r_{spl}))^2} \tag{34}$$

where $\epsilon$ is the depth of the potential well, and $r_0$ is the equilibrium distance. The inflection point $r_{spl}$ can be obtained by solving the following equation

$$\frac{\partial^2\psi}{\partial r^2}(r_{spl}) = 0. \tag{35}$$

A solution of $r_{spl}$ may be found as $r_{spl} = 1.244455r_0$. The cutoff distance is given by

$$r_{max} = r_{spl} - \frac{3\psi(r_{spl})}{2\frac{\partial\psi}{\partial r}(r_{spl})}. \tag{36}$$

A practical value of $r_{max}$ in numerical computation is found as $r_{max} = 1.547537r_0$. The electron density function is given by

$$\rho(r) = \begin{cases} \frac{\bar{\rho}_0}{d(d+1)}\left(\frac{r_{max}^2 - r^2}{r_{max}^2 - 1}\right)^2 & 0 < r < r_{max} \\ 0 & r_{max} \leqslant r \end{cases} \tag{37}$$

where $\bar{\rho} = \sum_j \rho(r_j)$; $\bar{\rho}_0 = 1/e$, and $d$ is the dimensionality.

Please cite this article in press as: Lyu D et al. A hierarchical multiscale cohesive zone model and simulation of dynamic fracture in metals. Engng Fract Mech (2016), http://dx.doi.org/10.1016/j.engfracmech.2016.06.005

For easy reference, the material parameters used in this example, the depth of the potential well $\epsilon$ and the equilibrium distance $r_0$ for Copper, are listed in Table 1, in which a comparison between the numerical value and the experimental measured value [33] is made.

*6.2.2. Barycentric finite element method and its quadrature rule*

In finite element implementation of the second example, linear triangular shape functions are adopted for the bulk element, bilinear quadrilateral shape functions with bubble mode are selected for the first-order process zone element, and shape functions for the hexagonal elements are employed in the second-order process zone. Implementing the hexagonal element and calculating the strain gradient field inside is not a trivial task. In this work, the 6-point honeycomb Wachspress element [34] is used to model the second-order process zone. The local finite element interpolation field is as follows:

$$\mathbf{u}(X,Y,t)=\sum_{I=1}^{6}N_I(\xi,\eta)\mathbf{u}_I(t) \tag{38}$$

Let $\Omega_e$ denote the regular hexagonal domain (see Fig. 14). The shape function $N_i$, corresponding to node $i$ is given by:

$$N_i(\xi,\eta)=c_i\frac{\lambda_{i+2}(\xi,\eta)\lambda_{i+3}(\xi,\eta)\lambda_{i+4}(\xi,\eta)\lambda_{i+5}(\xi,\eta)}{q(\xi,\eta)},\quad i=1,2,3,4,5,6 \tag{39}$$

where $\lambda_{i+1}(\xi,\eta)=0$ represents the line segment connecting $i$ and $i+1$. A circumference circle

$$q(\xi,\eta)=\xi^2+\eta^2-R^2=0 \tag{40}$$

encompasses the points of intersection of the extensions of the edge. The normalizing factor is defined as:

$$c_i=\frac{q(\xi_i,\eta_i)}{\lambda_{i+2}(\xi_i,\eta_i)\lambda_{i+3}(\xi_i,\eta_i)\lambda_{i+4}(\xi_i,\eta_i)\lambda_{i+5}(\xi_i,\eta_i)} \tag{41}$$

For the numerical integration of hexagonal element, the symmetric quadrature rules are adopted, which are proposed by Lyness and Monegato [35]. As illustrated in Fig. 15, the quadrature rule is invariant under 60° rotation due to the hexagonal symmetry of the integration region, which can be expressed:

$$\int_{\Omega_e}f d\Omega=\omega_0 f(0,0)+\sum_{j=1}^{N}\sum_{i=1}^{6}\omega_j f\left(r_j,\alpha_j+\frac{\pi i}{3}\right) \tag{42}$$

**Table 1**
Material parameters for copper.

| Parameter | Experiment | EAM-Holian |
|---|---|---|
| $C_{1111}$ [GPa] | 169 | 168.2 |
| $C_{1122}$ [GPa] | 122 | 117.5 |
| $C_{1212}$ [GPa] | 75.3 | 83.2 |
| $\epsilon$ [$eV$] | – | 0.43894774 |
| $r_0$ [$\AA$] | – | 2.57110688 |

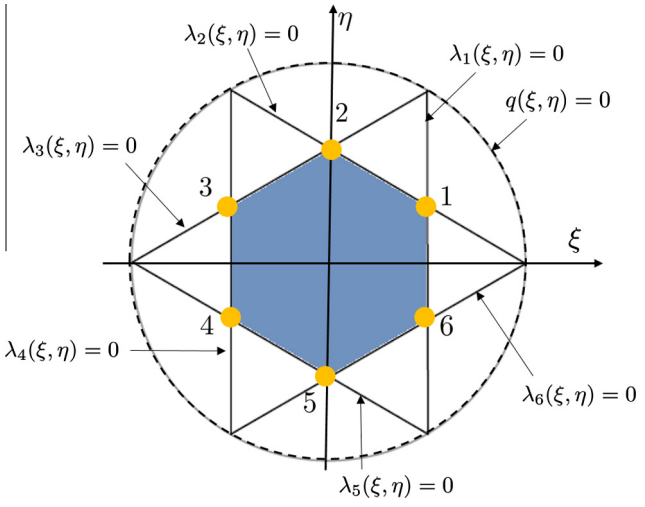


**Fig. 14.** The Washspress shape function for the honeycomb element.

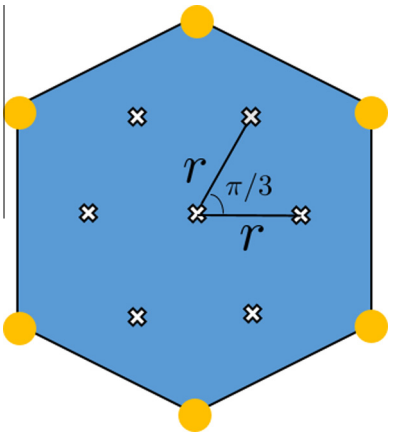


**Fig. 15.** Schematic illustration of the quadrature rule for the regular hexagonal element.

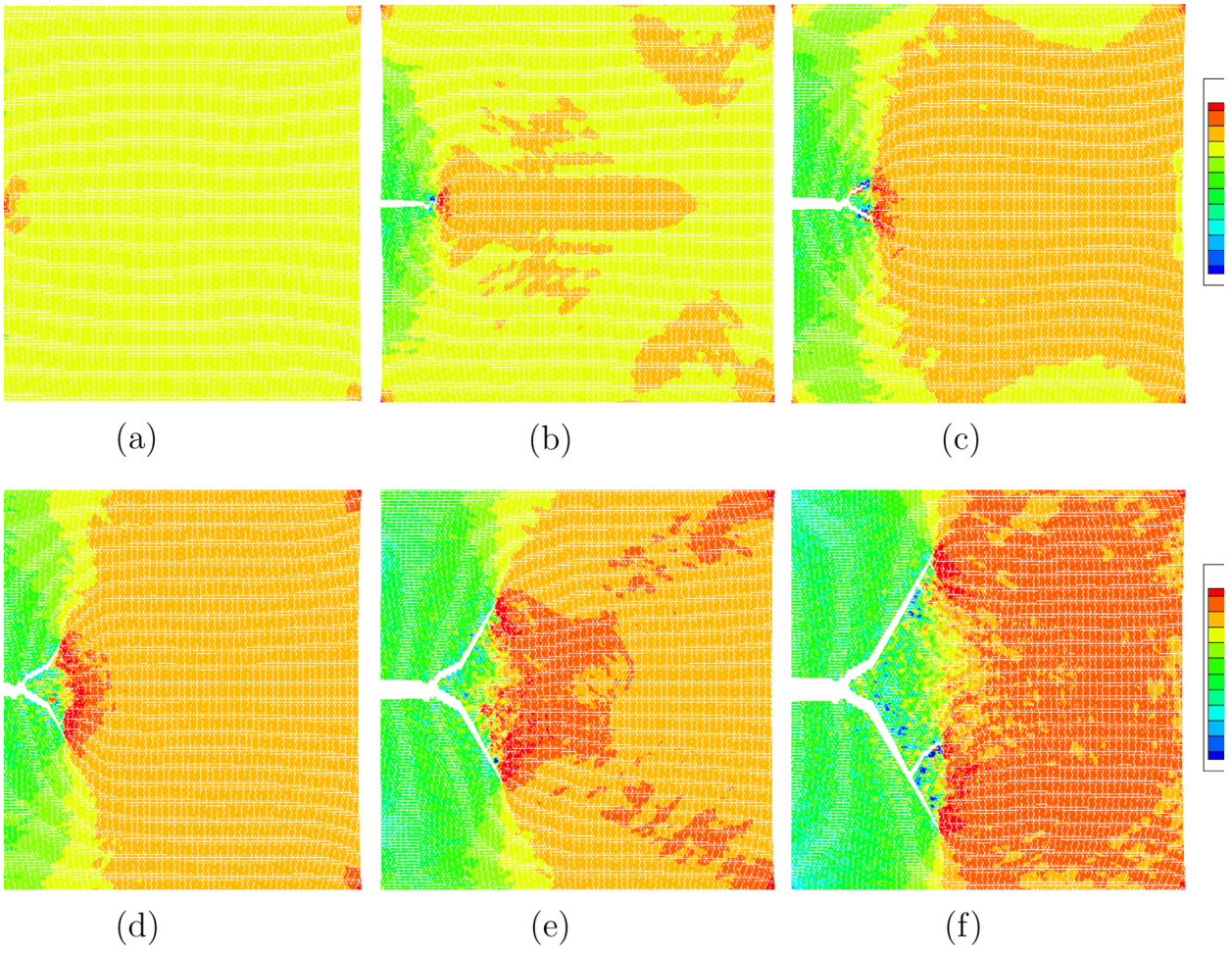


**Fig. 16.** Stress distributions in a crack propagation sequence.

where $\omega_j$ denotes the weight corresponding to the Gauss point at distance $r_j$ from the center of the hexagon and angle$\alpha_j + \frac{\pi i}{3}$ from the horizonal axis for $1 \leqslant i \leqslant 6$. In this work, $N = 1$ is chosen, which has 7 quadrature points including the point in the center, as shown in Fig. 15

Please cite this article in press as: Lyu D et al. A hierarchical multiscale cohesive zone model and simulation of dynamic fracture in metals. Engng Fract Mech (2016), http://dx.doi.org/10.1016/j.engfracmech.2016.06.005

The simulation domain is discretized into 82,212 nodes, 27,404 bulk elements, 40,873 first-order process zone elements, and 13,470 second-order process zone elements. Comparing with the full molecular dynamics simulation, the reduction ratio in the number of degrees of freedom is about 1-to-4. A pre-notched crack is set in the specimen, which has an initial length 30 in the reduced unit, the time increment of time integration is 0.0033, and the constant velocity applied at top and bottom is $0.03r_0/t$, which is consistent with the strain rate of $1.12 \times 10^{-4}$ in [31]. Fig. 16 shows the simulation results of stress distribution during crack propagation.

It is not difficult to find that at beginning the crack propagates horizontally and then it bifurcates due to the perturbation of acoustic wave reflected from the boundary. Moreover, Fig. 17 compares the crack speed history in this present work with that obtained in a MD simulation [31]. The agreement is very good except that process zone model predicts a slightly late crack growth.

### 6.3. Example III: Three-scale cohesive zone simulation of spall fracture

To further demonstrate the effectiveness of three-scale cohesive zone modeling, another numerical example is carried out, in which the proposed multiscale method is employed to simulate the dynamics spall fracture during high-speed impact and penetration process. The example setting is described in Fig. 18, in which a rigid projectile is penetrating a deformable plate under prescribed velocity. The projectile is a ($0.4\,\text{mm} \times 0.4\,\text{mm}$) rigid block with the prescribed impact velocity $v = 200$ m/s. The target is a ($2\,\text{mm} \times 0.4\,\text{mm}$) copper block clamped at the two side ends. Different from the second example, the multiscale finite element mesh contains three level rectangular elements, which are shown in the zooming region of Fig. 18.

Following [36], an EAM-Mishin potential is used to model the constitutive relation of the copper plate via higher order Cauchy–Born rule. The simulation time step is chosen to be $\Delta t = 1 \times 10^{-10}$ s. To solve the contact problem between the projectile and the copper plate during the impact and penetration process, the standard master–slave contact algorithm is adopted, in which the impenetrability condition is enforced for each element during every time step of the calculation, which is similar to the contact algorithm discussed in [37].

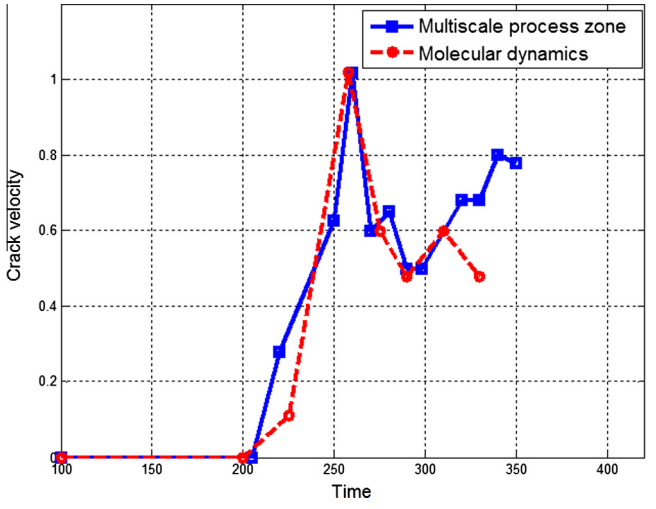


**Fig. 17.** Crack speed comparison between multiscale process zone model and molecular dynamics.

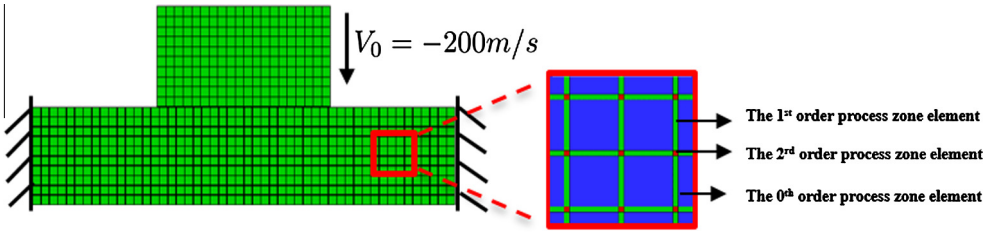


**Fig. 18.** Schematic illustration of Example 3 and multiscale process zone mesh.

Please cite this article in press as: Lyu D et al. A hierarchical multiscale cohesive zone model and simulation of dynamic fracture in metals. Engng Fract Mech (2016), http://dx.doi.org/10.1016/j.engfracmech.2016.06.005

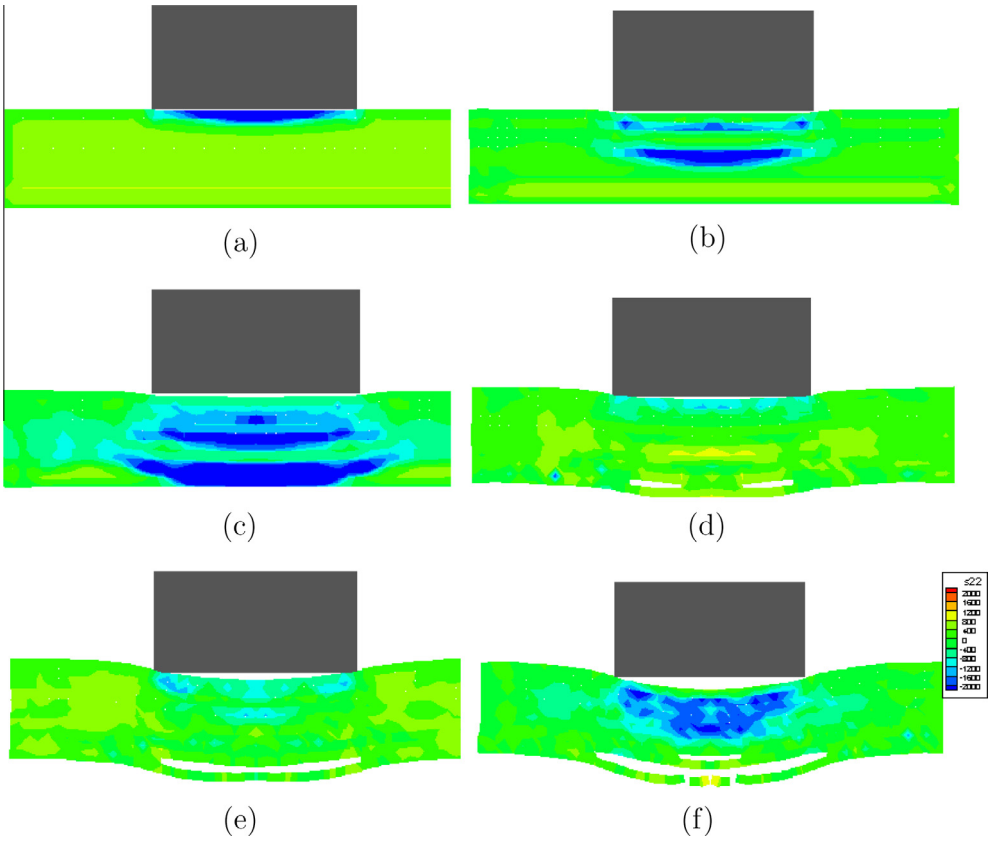


**Fig. 19.** Stress distributions in the copper plate during the contact-impact process.

The simulation results are shown in Fig. 19, in which a time sequence of the impact and penetration is plotted. One may find that due to the initial impact, a compressive stress wave propagates from the contact surface to the opposite boundary, and the subsequent spall fracture of the copper plate is clearly captured by the simulation (see Fig. 19).

## 7. Discussions and conclusions

In this work, a hierarchical multi-scale cohesive zone model (MCZM) is developed, and then employed to simulate dynamic fracture in crystalline and polycrystalline solids. The multi-scale cohesive model makes use of material information at atomistic scale, such as atomistic potential, lattice structure, and grain orientation in polycrystalline solids, to characterize constitutive relations. Thus, it is capable of capturing material inhomogeneities inside the process zone by incorporating the higher order Cauchy–Born rule in constitutive model. To include the effect of the nonlinear deformation on constitutive model, the higher order Cauchy–Born rules are adopted to obtain the expression of stress in the first-order and second-order process zone elements. In addition, to capture non-linear deformation mode, a bubble mode of finite element shape function is added into the quadrilateral element to support high order strain gradient effects, which enriches quadratic shape function basis in the conventional bilinear quadrilateral element. Subsequently, it substantiates the higher order Cauchy–Born rule based constitutive relations. To validate the multiscale cohesive zone model, numerical simulations of dynamics fracture are conducted in crystalline cooper specimen by using the proposed multiscale method with an EAM potential. A good agreement is found by comparing the simulation results of MCZM with that of the corresponding molecular dynamics simulation. In addition, we studied the effects of micro-structures with different grain sizes, mesh densities and cohesive zone strengthes on simulation results, and we investigated the influences of these factors on the fracture pattern when using the multiscale cohesive zone model to simulate fracture in polycrystalline solids. At lease in one example, the numerical simulation captures the transition from intergranular fracture to transgranular fracture during the crack propagation. Moreover, the method is successfully employed to simulate spall fracture of a copper plate under high-speed impact. In the third example, the FEM mesh has only 2000 nodes, which forms 500 bulk elements; 931 first order cohesive zone elements, and 441 second order cohesive zone elements. In total, it only has 1872 elements, and the total calculation only takes less than a few hours in a desktop computer depending on its speed. Therefore, MCZM can be a very efficient computational method.

Please cite this article in press as: Lyu D et al. A hierarchical multiscale cohesive zone model and simulation of dynamic fracture in metals. Engng Fract Mech (2016), http://dx.doi.org/10.1016/j.engfracmech.2016.06.005

Based on the numerical study presented in this paper, we conclude that the proposed hierarchical multiscale cohesive zone model provides a viable approach to study dynamic fracture in various crystalline solids from microscale to macroscale.

Last, we would like to point out that the main focus of the present work is to model the cohesive strength of crystalline solid materials by using a hierarchical multiscale cohesive zone model. The term strength used here is not just restricted to material tensile strength, but has a broader meaning, i.e. including both fracture toughness as well as ductility.

At macroscale, the concept of material ductility toughness implies plastic deformation. In the conventional cohesive zone model, the toughness part is described by the cohesive law in shear, which is in fact a numerical extension of the fracture model under small-scale yielding, i.e. the Dugdale–Barenblatt model [17,18]. On the other hand, at microscale, it is a public consensus now that one can use molecular dynamics to simulate ductile fracture by just employing the atomistic potentials.

In this work, we use exactly the same atomistic potentials that are used in molecular dynamics to conduct a multiscale cohesive strength modeling, which is essentially a mesoscale coarse grain approach. Therefore, it is attempting to make a definite statement that the higher-order Cauchy–Born based multiscale method can simulate ductile fracture, or the hierarchical multiscale cohesive zone model can capture the material ductile toughness. However, this is a far more profound problem than the study conducted in this work, and it is out the scope of this work.

To satisfactorily address this issue, one has to demonstrate that the proposed multiscale cohesive zone model can simulate aggregated dislocation motions, and the subsequent fracture process. In fact, we have reported some preliminary results on using the multiscale cohesive zone model to simulate aggregated dislocation motion in [36]. Example 3 reported in this paper is a study of ductile fracture at microscale. Based on these preliminary studies, the proposed hierarchical multiscale cohesive zone model may have certain abilities to simulate material toughness and ductile fracture.

## Appendix A

In this appendix, the third-order derivatives of the six-node honeycomb Wachspress shape function are provided. For the first-order and second-order derivatives of the six-node honeycomb Wachspress shape function, the readers may consult [38].

$$\frac{\partial^3 N_1}{\partial \xi^3} = -2h(\xi,\eta)\eta[-9+4\eta^2)(9\sqrt{3}+\sqrt{3}\eta^4+36\xi-4\eta^3\xi+18\sqrt{3}\xi^2+12\xi^3+\sqrt{3}\xi^4+4\eta\xi(3+\xi^2)-6\eta^2(\sqrt{3}+2\xi+\sqrt{3}\xi^2)]$$

$$\frac{\partial^3 N_1}{\partial \xi^2 \eta} = 2h(\xi,\eta)[4\eta^4(1+\sqrt{3}\xi)-2\eta^5(-5+8\xi^2)-18\eta(-3-2\xi^2+\xi^4)-3(-3+\xi^2)(9+9\sqrt{3}\xi+9\xi^2+\sqrt{3}\xi^3) + 16\eta^3(-3+\xi^2+\xi^4)+\eta^2(-54-54\sqrt{3}\xi+90\xi^2+66\sqrt{3}\xi^3+36\xi^4+4\sqrt{3}\xi^5)-\eta^4(3+3\sqrt{3}\xi+56\xi^2+24\sqrt{3}\xi^3)]$$

$$\frac{\partial^3 N_1}{\partial \xi \eta^2} = -2h(\xi,\eta)[16\eta^2\xi^3(-3+\xi^2)-6\xi(-3+\xi^2)(-3+\xi^2)+\eta^4(30\xi-16\xi^3)+\eta^3(-6\sqrt{3}+84\xi+38\sqrt{3}\xi^2-64\xi^3-24\sqrt{3}\xi^4) + \eta(-3+\xi^2)(-9\sqrt{3}+36\xi+27\sqrt{3}\xi^2+24\xi^3+4\sqrt{3}\xi^4)+\eta^5(-\sqrt{3}+8\xi+4\sqrt{3}\xi^2)]$$

$$\frac{\partial^3 N_1}{\partial \eta^3} = 2h(\xi,\eta)(-3+4\xi^2)[\eta^4(3+\sqrt{3}\xi)-4\eta^3(-3+\xi^2)+4\eta(-3+\xi^2)(-3+\xi^2)+(3+\sqrt{3}\xi)(-3+\xi^2)(-3+\xi^2) - 6\eta^2(3+\sqrt{3}\xi)(-3+\xi^2)]$$

$$\frac{\partial^3 N_2}{\partial \xi^3} = -h(\xi,\eta)[(8\eta(-3+2\eta)(3+2\eta)(3+2\eta)\xi(-3+\eta^2-\xi^2)]$$

$$\frac{\partial^3 N_2}{\partial \xi^2 \eta} = -2h(\xi,\eta)(3+2\eta)[2\eta^5+\eta^4(7-16\xi^2)-4\eta^3(3+\xi^2)-9(-3-2\xi^2+\xi^4)-6\eta(-3-2\xi^2+\xi^4) + 2\eta^2(-15+11\xi^2+8\xi^4)]$$

$$\frac{\partial^3 N_2}{\partial \xi \eta^2} = 8h(\xi,\eta)\xi[2\eta^5+\eta^3(21-16\xi^2)+\eta^4(15-8\xi^2)+8\eta^2\xi^2(-3+\xi^2)-3(-3+\xi^2)(-3+\xi^2)+3\eta(-9-3\xi^2+2\xi^4)]$$

$$\frac{\partial^3 N_2}{\partial \eta^3} = -h(\xi,\eta)[(2(-3+4\xi^2)(3\eta^4-18\eta^2(-3+\xi^2)-8\eta^3(-3+\xi^2)+3(-3+\xi^2)(-3+\xi^2)+8\eta(-3+\xi^2)(-3+\xi^2)]$$

$$\frac{\partial^3 N_3}{\partial \xi^3} = 2h(\xi,\eta)\eta(-9+4\eta^2)[9\sqrt{3}+\sqrt{3}\eta^4-36\xi+4\eta^3\xi+18\sqrt{3}\xi^2-12\xi^3+\sqrt{3}\xi^4-4\eta\xi(3+\xi^2)-6\eta^2(\sqrt{3}-2\xi+\sqrt{3}\xi^2)]$$

Please cite this article in press as: Lyu D et al. A hierarchical multiscale cohesive zone model and simulation of dynamic fracture in metals. Engng Fract Mech (2016), http://dx.doi.org/10.1016/j.engfracmech.2016.06.005

$$\frac{\partial^3 N_3}{\partial\xi^2\eta}=-2h(\xi,\eta)[4\eta^4(-1+\sqrt{3}\xi)+2\eta^5(-5+8\xi^2)+18\eta(-3-2\xi^2+\xi^4)+\eta^2(54-54\sqrt{3}\xi-90\xi^2+66\sqrt{3}\xi^3-36\xi^4+4\sqrt{3}\xi^5)$$
$$-3(-3+\xi^2)(-9+9\sqrt{3}\xi-9\xi^2+\sqrt{3}\xi^3)+\eta^4(3-3\sqrt{3}\xi+56\xi^2-24\sqrt{3}\xi^3)-16\eta^3(-3+\xi^2+\xi^4)]$$

$$\frac{\partial^3 N_3}{\partial\xi\eta^2}=2h(\xi,\eta)[-16\eta^2\xi^3(-3+\xi^2)+6\xi(-3+\xi^2)(-3+\xi^2)+\eta^3(-6\sqrt{3}-84\xi+38\sqrt{3}\xi^2+64\xi^3-24\sqrt{3}\xi^4)$$
$$+\eta(-3+\xi^2)(-9\sqrt{3}-36\xi+27\sqrt{3}\xi^2-24\xi^3+4\sqrt{3}\xi^4)+2\eta^4\xi(-15+8\xi^2)+\eta^5(-\sqrt{3}-8\xi+4\sqrt{3}\xi^2)]$$

$$\frac{\partial^3 N_3}{\partial\eta^3}=-2h(\xi,\eta)(-3+4\xi^2)[\eta^4(-3+\sqrt{3}\xi)+4\eta^3(-3+\xi^2)-4\eta(-3+\xi^2)(-3+\xi^2)+(-3+\sqrt{3}\xi)(-3+\xi^2)(-3+\xi^2)$$
$$-6\eta^2(-3+\sqrt{3}\xi)(-3+\xi^2)]$$

$$\frac{\partial^3 N_4}{\partial\xi^3}=-2h(\xi,\eta)\eta(-9+4\eta^2)[9\sqrt{3}+\sqrt{3}\eta^4-36\xi-4\eta^3\xi+18\sqrt{3}\xi^2-12\xi^3+\sqrt{3}\xi^4+4\eta\xi(3+\xi^2)-6\eta^2(\sqrt{3}-2\xi+\sqrt{3}\xi^2)]$$

$$\frac{\partial^3 N_4}{\partial\xi^2\eta}=2h(\xi,\eta)(4\eta^4[-1+\sqrt{3}\xi)-2\eta^5(-5+8\xi^2)-18\eta(-3-2\xi^2+\xi^4)-3(-3+\xi^2)(-9+9\sqrt{3}\xi-9\xi^2+\sqrt{3}\xi^3)$$
$$+16\eta^3(-3+\xi^2+\xi^4)+\eta^2(54-54\sqrt{3}\xi-90\xi^2+66\sqrt{3}\xi^3-36\xi^4+4\sqrt{3}\xi^5)+\eta^4(3-3\sqrt{3}\xi+56\xi^2-24\sqrt{3}\xi^3)]$$

$$\frac{\partial^3 N_4}{\partial\xi\eta^2}=-2h(\xi,\eta)[-16\eta^2\xi^3(-3+\xi^2)-6\xi(-3+\xi^2)(-3+\xi^2)+\eta^4(30\xi-16\xi^3)+\eta^3(-6\sqrt{3}-84\xi+38\sqrt{3}\xi^2+64\xi^3-24\sqrt{3}\xi^4)$$
$$+\eta(-3+\xi^2)(-9\sqrt{3}-36\xi+27\sqrt{3}\xi^2-24\xi^3+4\sqrt{3}\xi^4)+\eta^5(-\sqrt{3}-8\xi+4\sqrt{3}\xi^2)]$$

$$\frac{\partial^3 N_4}{\partial\eta^3}=2h(\xi,\eta)(-3+4\xi^2)[\eta^4(-3+\sqrt{3}\xi)-4\eta^3(-3+\xi^2)+4\eta(-3+\xi^2)(-3+\xi^2)+(-3+\sqrt{3}\xi)(-3+\xi^2)(-3+\xi^2)$$
$$-6\eta^2(-3+\sqrt{3}\xi)(-3+\xi^2)]$$

$$\frac{\partial^3 N_5}{\partial\xi^3}=-h(\xi,\eta)[(8(3-2\eta)(3-2\eta)\eta(3+2\eta)\xi(-3+\eta^2-\xi^2)]$$

$$\frac{\partial^3 N_5}{\partial\xi^2\eta}=2h(\xi,\eta)(-3+2\eta)[2\eta^5-4\eta^3(3+\xi^2)+\eta^4(-7+16\xi^2)-6\eta(-3-2\xi^2+\xi^4)-2\eta^2(-15+11\xi^2+8\xi^4)$$
$$+9(-3-2\xi^2+\xi^4)]$$

$$\frac{\partial^3 N_5}{\partial\xi\eta^2}=8h(\xi,\eta)\xi[-2\eta^5+\eta^4(15-8\xi^2)-3(-3+\xi^2)(-3+\xi^2)+\eta^3(-21+16\xi^2)+\eta(27+9\xi^2-6\xi^4)+8\eta^2\xi^2(-3+\xi^2)]$$

$$\frac{\partial^3 N_5}{\partial\eta^3}=2h(\xi,\eta)[(-3+4\xi^2)(3\eta^4-18\eta^2(-3+\xi^2)+8\eta^3(-3+\xi^2)+3(-3+\xi^2)(-3+\xi^2)-8\eta(-3+\xi^2)(-3+\xi^2)]$$

$$\frac{\partial^3 N_6}{\partial\xi^3}=2h(\xi,\eta)\eta(-9+4\eta^2)[9\sqrt{3}+\sqrt{3}\eta+36\xi+4\eta^3\xi+18\sqrt{3}\xi^2-4\eta\xi(3+\xi^2)-6\eta^2(\sqrt{3}+2\xi+\sqrt{3}\xi^2)+12\xi^3+\sqrt{3}\xi^4]$$

$$\frac{\partial^3 N_6}{\partial\xi^2\eta}=-2h(\xi,\eta)[4\eta^4(1+\sqrt{3}\xi)+2\eta^5(-5+8\xi^2)+36\xi^4+4\sqrt{3}\xi^5)-\eta^4(3+3\sqrt{3}\xi+56\xi^2+24\sqrt{3}\xi^3)+18\eta(-3-2\xi^2+\xi^4)$$
$$-16\eta^3(-3+\xi^2+\xi^4)-3(-3+\xi^2)(9+9\sqrt{3}\xi+9\xi^2+\sqrt{3}\xi^3)+\eta^2(-54-54\sqrt{3}\xi+90\xi^2+66\sqrt{3}\xi^3]$$

$$\frac{\partial^3 N_6}{\partial\xi\eta^2}=2h(\xi,\eta)[-16\eta^2\xi^3(-3+\xi^2)+6\xi(-3+\xi^2)(-3+\xi^2)+4\sqrt{3}\xi^2)+\eta^3(-6\sqrt{3}+84\xi+38\sqrt{3}\xi^2-64\xi^3-24\sqrt{3}\xi^4)$$
$$+\eta(-3+\xi^2)(-9\sqrt{3}+36\xi+27\sqrt{3}\xi^2+24\xi^3+4\sqrt{3}\xi^4)+\eta^5(-\sqrt{3}+8\xi+2\eta^4\xi(-15+8\xi^2)]$$

Please cite this article in press as: Lyu D et al. A hierarchical multiscale cohesive zone model and simulation of dynamic fracture in metals. Engng Fract Mech (2016), http://dx.doi.org/10.1016/j.engfracmech.2016.06.005

$$\frac{\partial^3 N_6}{\partial \eta^3} = -2h(\xi,\eta)(-3+4\xi^2)[\eta^4(3+\sqrt{3}\xi)+4\eta^3(-3+\xi^2)-4\eta(-3+\xi^2)(-3+\xi^2)+(3+\sqrt{3}\xi)(-3+\xi^2)(-3+\xi^2) - 6\eta^2(3+\sqrt{3}\xi)(-3+\xi^2)],$$

where $h(\xi,\eta)=\frac{1}{3}\left(\xi^2+\eta^2-3\right)^{-4}$.

## References

[1] Clayton JD. Modeling dynamic plasticity and spall fracture in high density polycrystalline alloys. Int J Solids Struct 2005;42:4613–40.
[2] Qian J, Li S. Application of multiscale cohesive zone model to simulate fracture in polycrystalline solids. J Eng Mater Technol 2011;133(1):11010.
[3] Espinosa HD, Zavattieri PD. A grain level model for the study of failure initiation and evolution in polycrystalline brittle materials. Part I: Theory and numerical implementation. Mech Mater 2003;35(3–6):333–64.
[4] Espinosa HD, Zavattieri PD. A grain level model for the study of failure initiation and evolution in polycrystalline brittle materials. Part II: Numerical examples. Mech Mater 2003;35:365–94.
[5] Bazant ZP, Asce F, Oh BH, Asce AM. Microplane model for progressive fracture of concrete and rock. J Eng Mech 1985;111(4):559–82.
[6] Addessio FL, Johnson JN. A constitutive model for the dynamic response of brittle materials. J Appl Phys 1990;67(7):3275.
[7] Curran DR, Seaman L, Cooper T, Shockey DA. Micromechanical model for comminution and granular flow of brittle material under high strain rate application to penetration of ceramic targets. J Impact Eng 1993;13(1):53–83.
[8] Espinosa HD. On the dynamic shear resistance of ceramic composites and its dependence on applied multiaxial deformation. Int J Solids Struct 1995;32(21):3105–28.
[9] Duddu R, Waisman H. A temperature dependent creep damage model for polycrystalline ice. Mech Mater 2012;46(Mar):23–41.
[10] Gurson AL. Continuum theory of ductile rupture by void nucleation and growth: Part—yield criteria and flow rules for porous ductile media. J Eng Mater Technol 1977;99:2–15.
[11] Lebensohn RA, Escobedo JP, Cerreta EK, Dennis-Koller D, Bronkhorst CA, Bingert JF. Modeling void growth in polycrystalline materials. Acta Mater 2013;61(18):6918–32.
[12] Lawn B. Fracture of brittle solid. Cambridge, UK: Cambridge University Press; 1993.
[13] Yuan XJ, Chen NX, Shen J, Hu W. Embedded-atom-method interatomic potentials from lattice inversion. J Phys Condens Matter: Inst Phys J 2010;22:375503.
[14] Schlick T. Molecular modeling and simulation: an interdisciplinary guide. New York, Inc., Secaucus: Springer-Verlag; 2002.
[15] Sfantos GK, Aliabadi MH. Multi-scale boundary element modelling of material degradation and fracture. Comput Methods Appl Mech Eng 2007;196(7):1310–29.
[16] Xu XP, Needleman A. Numerical simulations of fast crack growth in brittle solids. J Mech Phys Solids 1994;42:1397–434.
[17] Dugdale DS. Yielding of steel sheets containing slits. J Mech Phys Solids 1960;8(2):100–4.
[18] Barenblatt GI. The mathematical theory of equilibrium cracks in brittle fracture. Adv Appl Mech 1962;7:55–129.
[19] van den Bosch MJ, Schreurs PJG, Geers MGD. An improved description of the exponential Xu and Needleman cohesive zone law for mixed-mode decohesion. Eng Fract Mech 2006;73(9):1220–34.
[20] Zeng X, Li S. A multiscale cohesive zone model and simulations of fractures. Comput Methods Appl Mech Eng 2010;199(9–12):547–56.
[21] Li S, Zeng X, Ren B, Qian J, Zhang J, Jha AK. An atomistic-based interphase zone model for crystalline solids. Comput Methods Appl Mech Eng 2012;229–232(Jul):87–109.
[22] Zeng X, Li S. Application of a multiscale cohesive zone method to model composite materials. Int J Multiscale Comput Eng 2012;10(5):391–405.
[23] He M, Li S. An embedded atom hyperelastic constitutive model and multiscale cohesive finite element method. Comput Mech 2012;49(3):337–55.
[24] Liu L, Li S. A finite temperature multiscale interphase zone model and simulations of fracture. J Eng Mater Technol 2012;134(3):31014.
[25] Fan H, Li S. Multiscale cohesive zone modeling of crack propagations in polycrystalline solids. GAMM-Mitteilungen 2015;38(2):268–84.
[26] Ghosh S, Liu Y. Voronoi cell finite element model based on micropolar theory of thermoelasticity for heterogeneous materials. Int J Numer Methods Eng 1995;38(January 1994):1361–98.
[27] Bolander JE, Saito S. Fracture analyses using spring networks with random geometry. Eng Fract Mech 1998;61:569–91.
[28] Belytschko T, Ong JSJ, Liu WK, Kennedy JM. Hourglass control in linear and nonlinear problems. Comput Methods Appl Mech Eng 1984;43(3):251–76.
[29] Buban JP, Matsunaga K, Chen J, Shibata N, Ching WY, Yamamoto T, et al. Grain boundary strengthening in alumina by rare earth impurities. Science 2006;311:212–5.
[30] Lin L, Wang X, Zeng X. The role of cohesive zone properties on intergranular to transgranular fracture transition in polycrystalline solids. Int J Damage Mech 2015:1–16.
[31] Holian BL. Fracture simulations using large-scale molecular dynamics. Phys Rev B 1995;51(17):11275.
[32] Daw MS, Baskes MI. Embedded-atom method: derivation and application to impurities, surfaces, and other defects in metals. Physical Review B 1984;29:6443.
[33] Choy MM, Cook WR, Hearmon RFS, Jaff J, Jerphagnon J, Kurtz SK, et al. Landolt-bornstein: numerical data and functional relationships in science and technology new series. Group III: Crystal and Solid State Physics, Elastic, Piezoelectric, Pyroelectric, Piezooptic, Electrooptic Constants, and Nonlinear Dielectric Susceptibilities of Crystals, vol. 11. Berlin: Springer-Verlag; 1971.
[34] Talischi C, Paulino GH, Le CH. Honeycomb Wachspress finite elements for structural topology optimization. Struct Multidiscip Optim 2008;37(6):569–83.
[35] Lyness JN, Monegato G. Quadrature rules for regions having regular hexagonal symmetry. SIAM J Numer Anal 1977;14(2).
[36] Li S, Ren B, Minaki H. Multiscale crystal defect dynamics: a dual-lattice process zone model. Phil. Mag. 2014;94(13):1414–50.
[37] Hughes TJR, Taylor RL, Sackman JL, Curnier A, Kanoknukulchai W. A finite element method for a class of contact-impact problems. Comput Methods Appl Mech Eng 1976;8:249–76.
[38] Liu L, Li S. A multiscale crystal defect dynamics and its applications. In: Li S, Qian D, editors. Multiscale Simulations and Mechanics of Biological Materials. John Wiley Sons Ltd; 2013.

Please cite this article in press as: Lyu D et al. A hierarchical multiscale cohesive zone model and simulation of dynamic fracture in metals. Engng Fract Mech (2016), http://dx.doi.org/10.1016/j.engfracmech.2016.06.005